# $x_F$ dependence of $\psi$ and Drell-Yan production

R. Vogt

*Nuclear Science Division, Lawrence Berkeley National Laboratory, Berkeley, California 94720*
*and Physics Department, University of California at Davis, Davis, California 95616*
(Received 13 July 1999; published 14 February 2000)

We discuss the nuclear dependence of $\psi$ and $\psi'$ production in hadron-nucleus interactions as a function of longitudinal momentum fraction $x_F$. Nuclear effects such as final-state absorption, interactions with comovers, shadowing of parton distributions, energy loss, and intrinsic heavy-quark components are described separately and incorporated into the model which is then compared to the preliminary E866 data. The resulting nuclear dependence of Drell-Yan production at 800 GeV and proposed measurements of $\psi$, $\psi'$, and Drell-Yan production at 120 GeV are also calculated.

PACS number(s): 24.85.+p, 25.40.Ep

## I. INTRODUCTION

The factorization theorem of perturbative QCD [1] separates the perturbatively calculable short-distance quark and gluon interactions from the nonperturbative dynamics underlying the parton distribution functions in the hadron. The effectiveness of the factorization theorem in nuclear targets with mass number $A$ can be obtained by a comparison of the perturbative production cross sections of hard processes in nuclei to those in a free proton, or, since nuclear isospin effects are generally small, a nucleon. The dependence of particle production on atomic mass number $A$ is conventionally parameterized by a power law as [2–9]

$$\sigma_{pA} = \sigma_{pN} A^{\alpha}, \qquad (1)$$

where $\sigma_{pA}$ and $\sigma_{pN}$ are the integrated particle production cross sections in proton-nucleus and proton-nucleon interactions, respectively. If factorization is satisfied, then particle production should be independent of the presence of nuclear matter and $\sigma_{pA}$ would grow linearly with $A$, implying $\alpha = 1$. Drell-Yan production, integrated over all kinematic variables, shows this linear growth to rather high precision [2]. A number of experiments have measured a less than linear $A$ dependence for $\psi$ and $\psi'$ production [3–9]. Typical values of the exponent $\alpha$ in Eq. (1) are between 0.9 and 1. This nonlinear growth of the $\psi$ cross section with $A$ has been used to determine an effective nuclear absorption cross section [7,10,11] under the assumption that the deviation of $\alpha$ from unity is solely due to $\psi$ dissociation by nucleons. However, attributing the entirety of the integrated nuclear dependence to final-state absorption neglects other possible contributions, perhaps resulting in an overestimate of the nuclear absorption cross section. This paper identifies a number of possible nuclear effects on $\psi$ and, consequently, Drell-Yan production, and examines their contributions to Eq. (1).

Any dependence on the kinematic variables such as projectile energy or longitudinal momentum fraction, $x_F$, would reveal the importance of going beyond a simple $A$ scaling for production and a constant absorption cross section for $\psi$ production. Indeed, it has long been known that in quarkonium production $\alpha$ decreases as a function of $x_F$ [3–5]. There are a number of effects which could contribute to the $x_F$ dependence. The nuclear parton densities are systematically different from those in a deuteron or a free proton as a function of parton momentum fraction $x$ [12]. Such alterations of the parton densities are universal because they are independent of the final state, affecting both $\psi$ and Drell-Yan production. Another possible universal component is energy loss by the incoming parton as it traverses the nucleus [13,14]. The remaining mechanisms primarily affect $\psi$ and $\psi'$ production. Absorption of the produced $\psi$ or $c\bar{c}$ state by interactions with nucleons and/or produced particles has been claimed to be responsible for all $\psi$ suppression in nuclear collisions, at least up to $S+U$ interactions [10,11,15,16]. The importance of these absorption effects depends on the production mechanism and the magnitude of the interaction cross sections. Energy loss by the final-state color octet $c\bar{c}$ has also been suggested [17]. Finally, the presence of an intrinsic heavy-quark component of the projectile wave function is also considered [18,19].

We study the $x_F$ dependence using a two-component model employing concepts developed in Ref. [20]. The first component, based on perturbative QCD [21], is a hard-scattering approach that would yield an approximately linear $A$ dependence, as in dilepton production by the Drell-Yan mechanism. The $A$ dependent effects associated with hard scattering are final-state interactions, nuclear shadowing in the target, and energy loss in the projectile. The second component of the $x_F$ dependence arises from intrinsic $c\bar{c}$ pairs in the projectile wave function [18,19]. Since the charm quark mass is large, these intrinsic heavy quark pairs carry a significant fraction of the longitudinal momentum and contribute at large $x_F$, whereas perturbative production decreases strongly with $x_F$. The light spectator quarks in the intrinsic $c\bar{c}$ state interact on the nuclear surface, leading to an approximate $A^{2/3}$ dependence [19].

Such a separation of production mechanisms was first proposed by the NA3 Collaboration [3] when they divided their data into hard and diffractive components so that

$$\frac{d\sigma_{pA}}{dx_F} = A^{\alpha'} \frac{d\sigma_h}{dx_F} + A^{\beta} \frac{d\sigma_d}{dx_F}. \qquad (2)$$

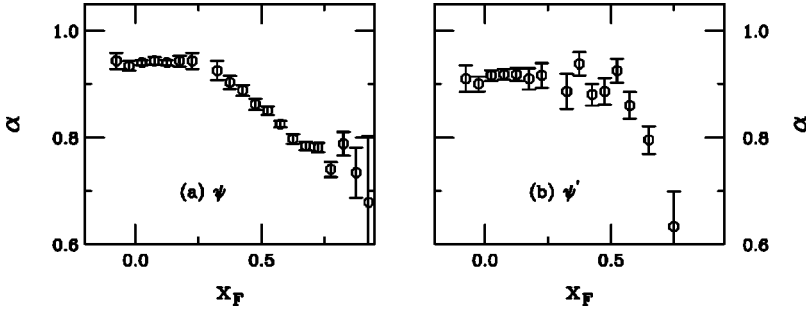The ''hard'' component, $\sigma_h$, includes nuclear shadowing

FIG. 1. The preliminary E866 data [9] for the $\psi$ and $\psi'$ $A$ dependence as a function of $x_F$.

and parton energy loss which can alter its effective $A$ dependence. Final state dissociation of the $\psi$ or $c\bar{c}$ state by nucleons and secondaries, which does not affect the parton densities, also contributes to the effective exponent $\alpha'$. The ''diffractive'' component, $\sigma_d$, is assumed to be due to intrinsic charm and only contributes significantly at $x_F > 0.25$. The NA3 Collaboration found $\alpha' = 0.97$ and $\beta = 0.71$ for proton projectiles [3]. Taken together, these components give the effective $\alpha$ of Eq. (1). We will discuss each mechanism in detail in the following sections. Since Drell-Yan production would also be affected by nuclear shadowing in the target and energy loss by the projectile partons, its effective $A$ dependence should also depend on $x_F$. Thus we will include the Drell-Yan $A$ dependence in our study.

We will calculate $\alpha(x_F)$ for each effect individually and then compare the shapes of $\alpha(x_F)$ with the preliminary E866 $\psi$ and $\psi'$ 800 GeV $pA$ data [9], shown in Fig. 1, when all the mechanisms are combined. For the $\psi$ $\alpha \approx 0.94$ until $x_F \approx 0.25$, decreasing to $\alpha \approx 0.7$ at large $x_F$ and for the $\psi'$ $\alpha \approx 0.91$, effectively constant, until $x_F \approx 0.5$. The two values of $\alpha$ are essentially compatible with each other within the experimental uncertainties. No decrease at negative $x_F$ is observed, contrary to previous results [6,8]. The drop to $\alpha \approx 0.7$ at $x_F \approx 0.9$ is similar to previous measurements [3,5]. Since the E866 targets are tungsten, W ($A = 184$), and beryllium, Be ($A = 9$), we calculate the cross section per nucleon for each target according to Eq. (2), obtaining from Eq. (1),

$$\alpha(x_F) = 1 + \frac{\ln[(d\sigma_{p\mathrm{W}}/A_{\mathrm{W}}dx_F)/(d\sigma_{p\mathrm{Be}}/A_{\mathrm{Be}}dx_F)]}{\ln(A_{\mathrm{W}}/A_{\mathrm{Be}})}. \quad (3)$$

We first discuss $\psi$ and Drell-Yan production in QCD and then each nuclear effect in turn. Quarkonium production by color evaporation and in nonrelativistic QCD is discussed in Sec. II and dilepton production by the Drell-Yan mechanism is briefly touched upon in Sec. III. Three different models of nuclear absorption are discussed in Sec. IV. The first two, absorption of pure color octet and color singlet states, respectively, are used in conjunction with the color evaporation model of quarkonium production. The last, a combination of octet and singlet absorption, is coupled to quarkonium production in nonrelativistic QCD. A discussion of quarkonium dissociation by comoving secondaries is presented in Sec. V. Three different parametrizations of nuclear shadowing are described in Sec. VI. Several models of energy loss are discussed in Sec. VII. The intrinsic charm model is introduced in Sec. VIII. The combined results are given in Sec. IX,

along with predictions for projected lower energy measurements at 120 GeV. A nontrivial combination of effects is required to understand the $\psi$ and $\psi'$ data.

## II. CHARMONIUM PRODUCTION

There are two basic models of quarkonium hadroproduction that have enjoyed considerable phenomenological success. The first, the color evaporation model, treats all charmonium production identically to $c\bar{c}$ production below the $D\bar{D}$ threshold. The more recent nonrelativistic QCD approach involves an expansion of quarkonium production in powers of $v$, the relative $Q$-$\bar{Q}$ velocity within the bound state. Each approach will be described in turn and the $x_F$ distributions in $pp$ interactions will be presented to provide a basis for understanding $d\sigma_h/dx_F$, Eq. (2), before nuclear effects are included. We will also show the relative contributions from $gg$ fusion, $q\bar{q}$ annihilation, and $gq$ scattering (in nonrelativistic QCD only).

### A. The color evaporation model

In the color evaporation model (CEM) quarkonium production is treated identically to open heavy-quark production except that the invariant mass of the heavy quark pair is restricted to be less than twice the mass of the lightest meson that can be formed with one heavy constituent quark. For charmonium the upper limit on the $c\bar{c}$ pair mass is then $2m_D$. The hadroproduction of heavy quarks at leading order (LO) in perturbative QCD is the sum of contributions from $q\bar{q}$ annihilation and $gg$ fusion. The hadroproduction cross section is a convolution of the $q\bar{q}$ and $gg$ partonic cross sections with the parton densities in projectile $A$ and target $B$. If $x_F$ is the $c\bar{c}$ longitudinal momentum fraction in the $AB$ center-of-mass frame and $\sqrt{s}$ is the center-of-mass energy of a nucleon-nucleon collision, the cross section for production of free $c\bar{c}$ pairs with mass $m$ is [22]

$$\frac{d\sigma^{c\bar{c}}}{dx_F dm^2} = \int_0^1 dx_1 dx_2 \ \delta(x_1 x_2 s - m^2)$$

$$\times \delta(x_F - x_1 + x_2) H_{AB}(x_1, x_2; m^2) \quad (4)$$

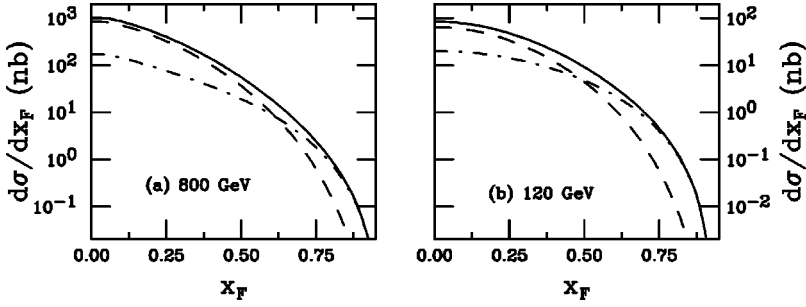$$= \frac{H_{AB}(x_{01}, x_{02}; m^2)}{\sqrt{x_F^2 s^2 + 4m^2 s}}, \quad (5)$$

FIG. 2. The $\psi\, x_F$ distributions at (a) 800 GeV and (b) 120 GeV in the CEM. The contributions from $gg$ fusion (dashed) and $q\bar{q}$ annihilation (dot-dashed) are given along with the total (solid).

where $x_1$ and $x_2$ are the fractions of the hadron momentum carried by the projectile and target partons, respectively. After integration over the delta functions in Eq. (4), $x_{01,02} = \frac{1}{2}(\pm x_F + \sqrt{x_F^2 + 4m^2/s})$. The convolution of the partonic cross sections [22,23] and the parton densities is

$$H_{AB}(x_1, x_2; m^2) = f_g^A(x_1, m^2) f_g^B(x_2, m^2) \sigma_{gg}(m^2)$$

$$+ \sum_{q=u,d,s} [f_q^A(x_1, m^2) f_{\bar{q}}^B(x_2, m^2)$$

$$+ f_{\bar{q}}^A(x_1, m^2) f_q^B(x_2, m^2)] \sigma_{q\bar{q}}(m^2),$$

(6)

where the parton densities $f_i(x, m^2)$ are evaluated at momentum fraction $x$ and scale $m^2 = x_1 x_2 s$, and $m$ is the invariant mass of the $c\bar{c}$ pair. The sum over $q$ includes only light quark flavors.

The LO charmonium cross section for charmonium state $i$, $\tilde{\sigma}_i$, is then obtained by integrating the free $c\bar{c}$ cross section over the pair mass from the $c\bar{c}$ production threshold, $2m_c$, to the open charm threshold, $2m_D = 3.74$ GeV. Then

$$\frac{d\tilde{\sigma}_i}{dx_F} = 2F_i \int_{2m_c}^{2m_D} m\, dm\, \frac{d\sigma^{c\bar{c}}}{dx_F dm^2},$$

(7)

where $F_i$ is the fraction of $\sigma^{c\bar{c}}$ that produces the final-state $c\bar{c}$ resonance.

The CEM assumes that the quarkonium dynamics are identical to those of low invariant mass $c\bar{c}$ pairs. The hadronization of the charmonium states from the $c\bar{c}$ pairs is nonperturbative, involving the emission of one or more soft gluons. A different nonperturbative matrix element is needed for the direct production of each charmonium state. Each nonperturbative matrix element is represented by a single universal factor $F_i$ which depends on the charm quark mass, $m_c$, the scale of $\alpha_s$, $\mu$, and the parton densities. In our calculations with the CEM, we use the leading order MRST LO parton distributions [24]. This set has a low initial $Q^2$, $Q_0 = 1$ GeV. The mass and scale parameters are $m_c = 1.2$ GeV and $\mu = 2m_c$. Once $F_i$ has been determined for each state, e.g., $\psi$, $\psi'$, or $\chi_{cJ}$, the model successfully predicts the energy and momentum dependencies. We note that $F_\psi$ includes both direct $\psi$ production and indirect production through radiative decays of the $\chi_{cJ}$ states and hadronic $\psi'$ decays.

Since $F_i$ must be a constant for the model to have any predictive power, the relative differential and integrated quarkonium production rates should be independent of projectile, target, and energy. This appears to be true for the charmonium production ratios $\Sigma_J \chi_{cJ}/\psi \approx 0.4$ and $\psi'/\psi \approx 0.14$ [25–28]. See Ref. [21] for more details.

The next-to-leading order (NLO) quarkonium production cross section in the CEM [21] was calculated using the $Q\bar{Q}$ production code of Ref. [29] with the mass cut in Eq. (7). When the NLO contribution is included, the $p_T$ dependence of $\psi$ production at the Tevatron has been shown to agree with the CEM calculations [30]. The LO and NLO calculations agree equally well with the energy and $x_F$ dependent data if $F_i^{LO}$ is defined as $F_i^{NLO}$ multiplied by a theoretical $K$ factor, the ratio of the NLO to LO cross sections [21]. At next-to-leading order, $F_\psi^{NLO}$ is 2.54% [21].

Figure 2 shows the forward $x_F$ distributions for $\psi$ production in $pp$ collisions[1] in the CEM at 800 and 120 GeV. The $\psi'$ distributions are identical except for the relative fraction of $\psi'$ production below the $D\bar{D}$ threshold and are thus not shown. Note that at large $x_F$, $x_F \gtrsim 0.6$ at 800 GeV and $\gtrsim 0.5$ at 120 GeV, $q\bar{q}$ annihilation is the most important contribution to the cross section.

**B. Quarkonium production in nonrelativistic QCD**

An alternative model of quarkonium production, the color singlet model [31], predicted that high $p_T$ $\psi$ production would be dominated by $\chi_{cJ}$ decays. It also predicted that direct $\psi$ and $\psi'$ production would be rare because a hard gluon emission was required to make a color singlet $^3S_1$ state on a perturbative time scale. On the other hand, the CEM is an average over the color and spin of the produced $c\bar{c}$ pair and cannot make such predictions. Soon after the high $p_T$ Tevatron data [32] made it clear that the hard gluon emission constraint in the color singlet model severely underpredicted direct $\psi$ and $\psi'$ production, the nonrelativistic QCD (NRQCD) approach to quarkonium production was formulated [33]. This approach does not restrict the angular momentum or color of the quarkonium state to only the leading singlet state. For example, the final-state $\psi$ may be produced as a $^3P_0$ color octet state which becomes a $\psi$ through nonperturbative soft gluon emissions. Thus the NRQCD

_____

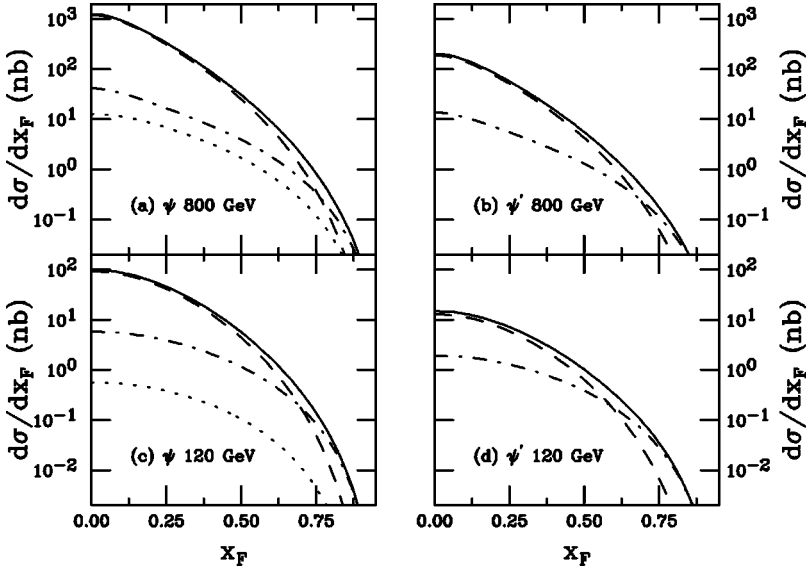[1]The $x_F$ distributions are symmetric around $x_F = 0$ in $pp$ production.

FIG. 3. The $\psi x_F$ distributions at (a) 800 GeV and (c) 120 GeV in NRQCD. The contributions from $gg$ fusion (dashed), $q\bar{q}$ annihilation (dot-dashed), $gq$ scattering (dotted), and the total (solid) are given. The corresponding $\psi'$ distributions are given in (b) and (d). The curves show $gg$ fusion (dashed), $q\bar{q}$ annihilation (dot-dashed), and the total (solid).

model is similar in spirit to the CEM albeit with more non-perturbative parameters, as we will see.

The $x_F$ distribution of a charmonium state, $C$, in NRQCD is

$$\frac{d\sigma^C}{dx_F} = \sum_{i,j} \int_0^1 dx_1 dx_2 \delta(x_F - x_1$$

$$+ x_2) f_i^A(x_1, \mu^2) f_j^B(x_2, \mu^2) \hat{\sigma}(ij \to C) \quad (8)$$

$$\hat{\sigma}(ij \to C) = \sum_n C_{Q\bar{Q}[n]}^{ij} \langle \mathcal{O}_n^C \rangle, \quad (9)$$

where the $C$ production cross section, $\hat{\sigma}(ij \to C)$, is the product of expansion coefficients, $C_{Q\bar{Q}[n]}^{ij}$, calculated perturbatively in powers of $\alpha_s(\mu^2)$ and nonperturbative parameters, $\langle \mathcal{O}_n^C \rangle$, describing the hadronization of the charmonium state. In the model, $\chi_{c0}$ and $\chi_{c2}$ are produced as color singlets by $gg$ fusion and as color octets through $q\bar{q}$ annihilation, both with $C_{Q\bar{Q}[n]}^{ij} \propto \alpha_s^2$. The three $\chi_{cJ}$ states, the $\psi$, and $\psi'$ are all produced as color octets through $q\bar{q}$ annihilation with $C_{Q\bar{Q}[n]}^{ij} \propto \alpha_s^2$. Direct $\psi$ and $\psi'$ occurs through gluon fusion both in color octet production with $C_{Q\bar{Q}[n]}^{ij} \propto \alpha_s^2$ and in color singlet production with $C_{Q\bar{Q}[n]}^{ij} \propto \alpha_s^3$. In addition, the $\chi_{c1}$ can be produced as a color singlet through $gg$ fusion and $g(q+\bar{q})$ scattering with $C_{Q\bar{Q}[n]}^{ij} \propto \alpha_s^2$. For charmonium production proportional to $\alpha_s^2$, an additional delta function enters Eq. (8) so that $x_1$ and $x_2$ are both fixed as in Eq. (2). However, when the expansion coefficients are proportional to $\alpha_s^3$, only $x_1$ or $x_2$ can be fixed by the delta function in Eq. (8), while the other momentum fraction must be integrated over. We use the parameters determined by Beneke and Rothstein [34] for fixed-target hadroproduction of charmonium with $m_c = 1.5$ GeV and $\mu = 2m_c$, and the CTEQ 3L parton densities [35].

The total $\psi$ $x_F$ distribution includes radiative decays of the $\chi_{cJ}$ states and hadronic decays of the $\psi'$,

$$\frac{d\sigma_\psi}{dx_F} = \frac{d\sigma_\psi^{\text{dir}}}{dx_F} + \sum_{J=0}^2 B(\chi_{cJ} \to \psi X) \frac{d\sigma_{\chi_{cJ}}}{dx_F} + B(\psi' \to \psi X) \frac{d\sigma_{\psi'}}{dx_F}. \quad (10)$$

In contrast, in the CEM, the $x_F$ distributions of all states are assumed to be the same. Thus $F_\psi$ in Eq. (7) implicitly includes the $\chi_{cJ}$ and $\psi'$ decay contributions given explicitly in Eq. (10). See Ref. [34] for the expressions for the charmonium cross sections and the values of the nonperturbative parameters $\langle \mathcal{O}_n^C \rangle$.

In Ref. [34], the singlet matrix elements were calculated from the quarkonium wave functions at the origin. The octet matrix elements were fit to Tevatron production data except for $\Delta_8$ [34] which was obtained from a fit to total cross sections data at fixed-target energies. In NRQCD, three parameters are needed to fix the $\psi'$ production cross section, while eight are needed for the total $\psi$ cross section. Only one parameter for each state is needed in the CEM, a considerable reduction.

The total $\psi$ forward $x_F$ distributions[2] at 800 and 120 GeV, Eq. (10), are shown in Figs. 3(a) and 3(c), respectively. Since the $\chi_{c0}$ branching ratio to $\psi$ is less than 1%, its contribution is virtually negligible. However, $\approx 27\%$ of the produced $\chi_{c1}$ states decay to $\psi$, including the $gq$ scattering contribution, are shown in the dotted curves. At 800 GeV this component is only a factor of 2–3 less than the total $q\bar{q}$ contribution to the full $\psi$ cross section. The $gg$ contribution from $\chi_{c1}$ decays and the smaller $\chi_{c2}$ decay contribution, $\approx 14\%$, provide most of the singlet component of total $\psi$ production. Interestingly, when the $\chi_{cJ}$ decays are included, the octet contribution to the total $\psi$ production cross section is 60%, close to

_____

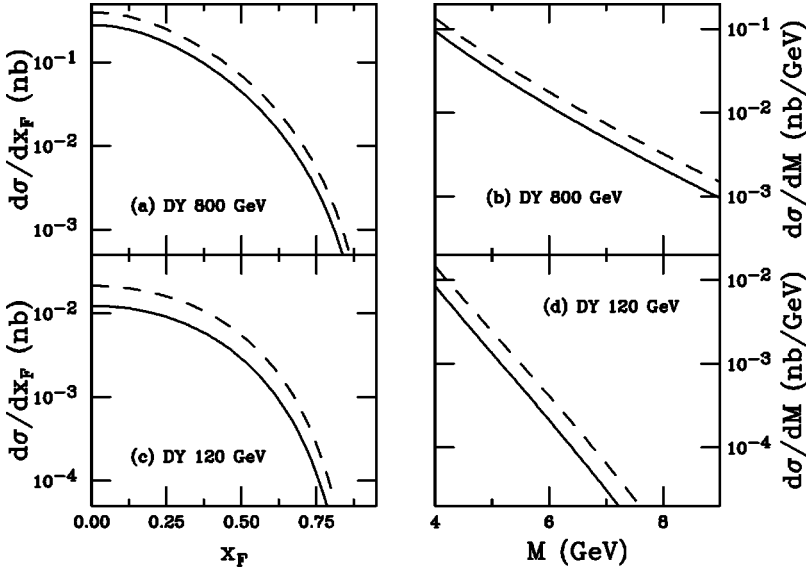[2]Note that, as in the CEM, the $pp$ $x_F$ distributions are symmetric around $x_F = 0$.

FIG. 4. The Drell-Yan $x_F$ distributions for $4 < M < 9$ GeV at (a) 800 GeV and (c) 120 GeV. The Drell-Yan mass distributions, integrated over $x_F$ are shown in (b) and (d) at 800 and 120 GeV, respectively. The leading order results are given by the solid curves, the next-to-leading order results are shown in the dashed curves.

the $\psi'$. At 120 GeV, the percentage of octet production is larger for both the total $\psi$ and $\psi'$, 67 and 78 %, respectively. The $\psi'$ $x_F$ distributions at 800 and 120 GeV are given in Figs. 3(b) and 3(d), including the individual contributions from $gg$ fusion and $q\bar{q}$ annihilation. Here the $q\bar{q}$ contribution is largest at $x_F \approx 0.7$ at 800 GeV and $\approx 0.6$ at 120 GeV, similar to the CEM. However, for the total $\psi$ $x_F$ distribution, the $q\bar{q}$ contribution is significantly smaller than in the CEM, resulting in a narrower $\psi$ $x_F$ distribution in NRQCD. The NRQCD cross section is a factor of 3 smaller than the CEM cross section at $x_F \approx 0.9$ and a factor of 1.5 smaller at $x_F \approx 0.5$ where the two are equal at $x_F = 0$. The $q\bar{q}$ component does not dominate the total $\psi$ distribution until $x_F \approx 0.8$ at 800 GeV and $\approx 0.7$ at 120 GeV. These relative differences can influence the strength of nuclear effects that depend on the nuclear quark and gluon distributions.

## III. DRELL-YAN PRODUCTION

Lepton pairs are produced by the Drell-Yan process, $q\bar{q}$ annihilation into a virtual photon at leading order, $q\bar{q} \rightarrow \gamma^\star \rightarrow l^+ l^-$ [36]. The partonic cross section for Drell-Yan production is

$$\frac{d\hat{\sigma}}{dM} = \frac{8\pi\alpha^2}{9M} e_q^2 \delta(\hat{s} - M^2), \tag{11}$$

where $\hat{s} = x_1 x_2 s$. To obtain the hadroproduction cross section as a function of pair mass, $M$, and $x_F$, we must fold the partonic cross section with the quark and antiquark densities evaluated at $M$, taken here to be in the range $4 < M < 9$ GeV, between the $\psi$ and $\Upsilon$ family regions. Then

$$\frac{d\sigma^{DY}}{dx_F dM} = \frac{8\pi\alpha^2}{9M} \int_0^1 dx_1 dx_2 \, \delta(x_1 x_2 s - M^2) \, \delta(x_F - x_1 + x_2)$$

$$\times \sum_q e_q^2 [f_q^p(x_1, M^2) f_{\bar{q}}^A(x_2, M^2)$$

$$+ f_{\bar{q}}^p(x_1, M^2) f_q^A(x_2, M^2)]. \tag{12}$$

After integrating the delta functions, the LO cross section, including the isospin of the target nucleus, is

$$\frac{d\sigma^{DY}}{dx_F dM} = \frac{8\pi\alpha^2}{9M} \frac{1}{\sqrt{x_F^2 s^2 + 4M^2 s}} \sum_q e_q^2 [f_q^p(x_{01}, M^2)$$

$$\times (z_A f_{\bar{q}}^p(x_{02}, M^2) + n_A f_{\bar{q}}^n(x_{02}, M^2))$$

$$+ f_{\bar{q}}^p(x_{01}, M^2)(z_A f_q^p(x_{02}, M^2) + n_A f_q^n(x_{02}, M^2))], \tag{13}$$

where $z_A = Z/A$ and $n_A = N/A$ are, respectively, the fractions of protons and neutrons in the target nucleus.

When this leading order cross section is compared to data, it falls short by an approximately constant factor, known as the $K$ factor. Experimentally, it is $\approx 1.7 - 2.5$, depending on the energy, mass range, and parton distribution functions. At NLO, the Compton and annihilation processes, $qg \rightarrow q\gamma^\star$ and $q\bar{q} \rightarrow g\gamma^\star$, respectively contribute, in addition to virtual corrections, to the LO cross section, resulting in a theoretical $K$ factor — the ratio of the NLO to the LO cross sections — of approximately $1.4 - 2$, somewhat less than that obtained by comparison to the data [36]. This theoretical $K$ factor serves the same purpose as the adjustment of $F_\psi$ between the LO and NLO calculations in the CEM, discussed earlier.

In Figs. 4(a) and 4(c) the Drell-Yan $x_F$ distribution is shown for masses between 4 and 9 GeV at 800 and 120 GeV. The 120 GeV $x_F$ distribution does not extend over all $x_F$ since the phase space for high $x_F$ and high mass pairs becomes limited. Because the quark distributions have a harder $x$ dependence than the gluon, the Drell-Yan $x_F$ distribution is broader than the $\psi$ $x_F$ distributions shown in Figs. 2 and 3. For comparison, both the LO and the NLO distributions are shown. There is some dependence of the $K$ factor on $x_F$. At 800 GeV and $x_F \sim 0$, the theoretical $K$ factor is 1.4, increasing to 2.1 at $x_F = 0.9$. The calculated $K$ factor is 20% larger at 120 GeV. The change with $x_F$ reflects the increasing importance of the Compton process with increasing $x_F$, corresponding to an increase in the gluon density at low $x_2$. The

Drell-Yan mass distribution, integrated over the corresponding $x_F$ ranges given in Figs. 4(a) and 4(c), is shown in Figs. 4(b) and 4(d) at 800 and 120 GeV, respectively. Since $x_F$ is integrated over, the lower $x_F$ values are the most important for the determination of the $K$ factor as a function of mass. The theoretical $K$ factor is $\approx 1.4$ at 800 GeV and 1.8 at 120 GeV, and does not change more than a few percent with mass.

Since the Drell-Yan mechanism produces lepton pairs which only interact electroweakly, the $A$ dependence is expected to be weak because no final-state interactions affect the lepton pair. However, initial-state interactions such as shadowing and energy loss may influence the $A$ dependence, as we discuss in Secs. VI and VII.

## IV. NUCLEAR ABSORPTION IN $pA$ INTERACTIONS

The $c\bar{c}$ pair may interact with nucleons and be dissociated or absorbed before it can escape the target. The effect of nuclear absorption alone on the $\psi$ production cross section in $pA$ collisions may be expressed as [23]

$$\sigma_{pA} = \sigma_{pN} \int d^2b \int_{-\infty}^{\infty} dz \, \rho_A(b,z) S^{\text{abs}}(b) \tag{14}$$

$$= \sigma_{pN} \int d^2b \int_{-\infty}^{\infty} dz \, \rho_A(b,z)$$

$$\times \exp\left\{ -\int_z^{\infty} dz' \rho_A(b,z') \sigma_{\text{abs}}(z'-z) \right\}, \tag{15}$$

where $b$ is the impact parameter, $z$ is the $c\bar{c}$ production point, $S^{\text{abs}}$ is the nuclear absorption survival probability, and $\sigma_{\text{abs}}$ is the charmonium [or $(c\bar{c})_8 g$ [37]] nucleon absorption cross section. Nuclear charge density distributions from data are used for $\rho_A$ [38]. Note that expanding the exponent in Eq. (15), integrating, and reexponentiating the results assuming $A$ is large leads to Eq. (1) with $\alpha = 1 - 9\sigma_{\text{abs}}/(16\pi r_0^2)$ [23].

We study three different models of nuclear absorption: either all quarkonium states are produced as color octets or color singlets or as a combination of octet and singlet states. When pure octet or pure singlet absorption is considered, $\psi$ and $\psi'$ production are calculated in the CEM. When a combination of octet and singlet absorption is assumed, NRQCD is used to obtain the correct balance between octet and singlet production. Both the CEM and NRQCD model parameters are tuned to fit $pp$ production. In this section, we only give examples of a range of cross sections for each absorption model. The actual values of $\sigma_{\text{abs}}$ are set in Sec. IX after initial state effects have also been included.

In our considerations of $\psi$ absorption, we include the $\approx 30\%$ contribution from $\chi_{cJ}$ decays [25] and the $\approx 12\%$ contribution from $\psi'$ decays [21]. Then the total $\psi$ survival probability, including indirect production, is

$$S_\psi^{\text{abs}}(b) = 0.58 S_{\psi,\text{dir}}^{\text{abs}}(b) + 0.3 S_{\chi_{cJ}}^{\text{abs}}(b) + 0.12 S_{\psi'}^{\text{abs}}(b). \tag{16}$$

The $\psi'$ itself is only produced directly since other, more massive, charmonium resonances decay to $D\bar{D}$ pairs.

The first case is pure octet production. Here, the $c\bar{c}$ is produced in a color octet state, $(c\bar{c})_8$, which travels through the nucleus. As it leaves the field of the nucleon that produced it, it neutralizes its color by combining with a collinear gluon in a nonperturbative interaction. The resulting $(c\bar{c})_8 g$ state is a color singlet as it traverses the nucleus. The final-state charmonium resonance will be formed when the accompanying gluon is absorbed by the $(c\bar{c})_8$ state. When the $(c\bar{c})_8 g$ state interacts with nucleons, a gluon is exchanged which can couple to either the $g$ or the $(c\bar{c})_8$, leaving the remaining state colored. Since this colored state is not yet bound, any interaction can lead to the break up of the state. There is thus no energy dependent threshold for $\psi$ breakup in this description. Because the initial color octet is the same regardless of the eventual final-state resonance, $\sigma_{\text{abs}} = \sigma_{\psi N}^o = \sigma_{\psi' N}^o = \sigma_{\chi_{cJ} N}^o$. Therefore $S_{\text{oct}}^{\text{abs}} = S_{\psi,\text{dir, oct}}^{\text{abs}} = S_{\chi_{cJ},\text{oct}}^{\text{abs}} = S_{\psi',\text{oct}}^{\text{abs}}$ and the feed-down contributions to the $\psi$ in Eq. (16) do not affect the absorption. The time needed for the formation of the final-state resonance is $\tau_8 \sim 0.3$ fm in the $(c\bar{c})_8$ rest frame during which the state travels a distance $d_8 \sim \tau_8 \cosh(y_{\text{cm}} + y_\psi)$ in the rest frame of the target. This distance is large enough that the color neutralization takes place outside large nuclear targets at 800 GeV.

The octet cross section has typically been assumed to be energy independent because the $\psi A$ dependence seems to be independent of projectile energy. This assumption has been used in most models of $\psi$ suppression in nuclear collisions [23]. While this apparent energy independence has been attributed to nuclear absorption alone, it could be caused by a convergence of competing effects. For the sake of clarity, we assume $\sigma_{\psi N}^o$ is a constant, independent of energy and $x_F$ and treat absorption as if only the $(c\bar{c})_8 g$ interacts with nucleons, not the final charmonium states. In Fig. 5(a), $\alpha$ is given for several values of the $(c\bar{c})_8 g$ cross section: $\sigma_{\text{abs}} = 1$, 3, 5, and 7 mb corresponding to $\alpha = 0.98$, 0.95, 0.92, and 0.90 respectively. It is obvious that octet production alone will not modify the shape of $\alpha$ as a function of $x_F$.

We now discuss absorption when all $c\bar{c}$ pairs are produced as color singlets. If the $c\bar{c}$ pair is produced as a color singlet, it is initially small with a spatial extent on the order of its production time, $\tau \propto m_c^{-1}$, ignored in the calculation. The proper time required for the formation of the final charmonium bound state obtained from potential models [39], $\tau_\psi \sim 1-2$ fm, is considerably longer. The $c\bar{c}-N$ absorption cross section may be expected to grow as a function of proper time until $\tau_{\psi_i}$ when it saturates at the asymptotic value $\sigma_{\psi_i N}^s$. We simulate the growth of the absorption cross section by [15,40]

$$\sigma_{\text{abs}}(z'-z) = \begin{cases} \sigma_{\psi_i N}^s \left(\dfrac{\tau}{\tau_{\psi_i}}\right)^\kappa & \text{if} \quad \tau < \tau_\psi \\ \sigma_{\psi_i N}^s & \text{otherwise.} \end{cases} \tag{17}$$
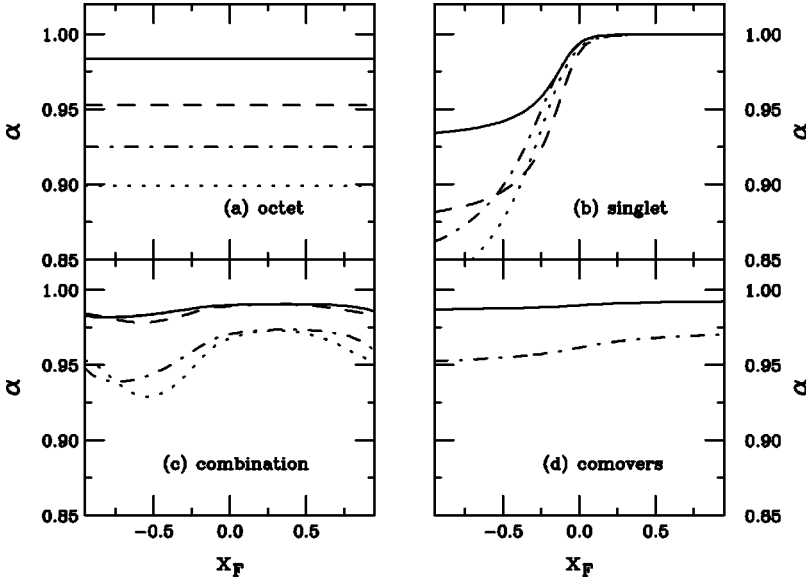
FIG. 5. The $A$ dependence of nuclear absorption models is given in (a), (b), and (c), and the comover $A$ dependence is shown in (d). In (a), octet cross sections of 1 mb (solid), 3 mb (dashed), 5 mb (dot-dashed), and 7 mb (dotted) are shown. Singlet absorption is shown in (b) for $\psi$ with $\sigma_{\psi N}^s = 5$ mb (solid) and 10 mb (dashed), as well as $\psi'$ with $\sigma_{\psi' N}^s = 15$ mb (dot-dashed) and 20 mb (dotted). A combination of octet and singlet production is assumed in (c). The curves represent $\psi$ absorption with $\sigma_{abs}^{oct} = 1$ mb and $\sigma_{abs}^{sing} = 1$ mb (solid), and $\sigma_{abs}^{oct} = 3$ mb and $\sigma_{abs}^{sing} = 5$ mb (dot-dashed); $\psi'$ absorption with $\sigma_{abs}^{oct} = 1$ mb and $\sigma_{abs}^{sing} = 3.7$ mb (dashed), and $\sigma_{abs}^{oct} = 3$ mb and $\sigma_{abs}^{sing} = 19$ mb (dotted). In (d), comover interactions are shown for $\sigma_{\psi co} = 0.67$ mb (solid) and $\sigma_{\psi' co} = 3.7 \sigma_{\psi co}$ (dot-dashed).

The exponent $\kappa$ determines the increase of $\sigma_{abs}$ during hadronization of the $c\bar{c}$ pair. If $\sigma_{abs}$ is proportional to the geometric cross section, then we expect $\kappa \sim 2$. [See also [41] for predictions of $\sigma_{\psi N}^s$ if $\kappa = 1$.] The proper time $\tau$ is related to the path length traversed by the $c\bar{c}$ pair through nuclear matter, $\tau = (z' - z)/\gamma v$. The $\gamma$ factor introduces $x_F$ and energy dependencies in the growth of the cross section. Depending on the initial energy of the projectile and the size of the target, the $c\bar{c}$ pair may form a $\psi$ inside or outside of the target.

In Fig. 5(b), examples of $\alpha$ are given for direct $\psi$ and $\psi'$ absorption at 800 GeV. The solid and dashed curves assume $\sigma_{\psi N}^s = 5$ and 10 mb, respectively, while the dot-dashed and dotted curves are for $\sigma_{\psi' N}^s = 15$ and 20 mb. In our calculations, we assume that the asymptotic absorption cross sections scale in proportion to the squares of the charmonium radii [42], $\sigma_{\psi' N}^s \approx 3.7 \sigma_{\psi N}^s$ and $\sigma_{\chi_{cJ} N}^s \approx 2.4 \sigma_{\psi N}^s$. Thus each contribution to Eq. (16) has a different $A$ dependence where typically $S_{\psi, dir, sing}^{abs} > S_{\psi', sing}^{abs}$. The $\psi$ and $\psi'$ formation times are different, $\tau_\psi = 0.92$ fm and $\tau_{\psi'} = 1.5$ fm [39]. The $\psi$ and $\psi'$ results at $x_F < 0$ in Fig. 5(b) reflect the differences in formation times as well as the gamma shift due to their masses. At 800 GeV, by $x_F = 0$ the final-state meson is produced outside the target so that $\alpha \approx 1$ for $x_F > 0$. Therefore, the $A$ dependence of color singlet production is virtually independent of $\sigma_{\psi_i N}^s$ for $x_F > 0$ at 800 GeV. At 120 GeV, both states can be produced inside the target at $x_F > 0$ and influence the $A$ dependence at forward $x_F$ as well.

More realistically, $\psi$ production is a combination of octet and singlet states, as in NRQCD. The ratio of octet to singlet production is energy and $x_F$ dependent [34] so that the relative absorption of each state depends on $x_F$ since the octet and singlet absorption cross sections are expected to be different [43]. Because the $\psi'$ is directly produced, the $x_F$ dependence of absorption is straightforward,

$$\frac{d\sigma_{pA}^{\psi'}}{dx_F} = \frac{d\sigma_{pp}^{\psi', oct}}{dx_F} \int d^2b\, dz\, S_{oct}^{abs}(b)$$
$$+ \frac{d\sigma_{pp}^{\psi', sing}}{dx_F} \int d^2b\, dz\, S_{\psi', sing}^{abs}(b), \qquad (18)$$

where $\sigma_{abs}^{oct}$ and $\sigma_{abs}^{sing}$ replace $\sigma_{abs}$ in Eq. (15). The $\psi$ distribution is more complicated since we must account for the fact that the octet absorption cross section is independent of the charmonium state while the singlet cross sections are not. In the octet case, the same $S_{oct}^{abs}$ can be applied to all states feeding the $\psi$, while singlet absorption is different for each individual state. Then,

$$\frac{d\sigma_{pA}^{\psi, tot}}{dx_F} = \left[ \frac{d\sigma_{pp}^{\psi, dir, oct}}{dx_F} + \sum_{J=0}^{2} B(\chi_{cJ} \rightarrow \psi X) \frac{d\sigma_{pp}^{\chi_{cJ}, oct}}{dx_F} \right.$$
$$+ B(\psi' \rightarrow \psi X) \frac{d\sigma_{pp}^{\psi', oct}}{dx_F} \right] \int d^2b\, dz S_{oct}^{abs}(b)$$
$$+ \int d^2b\, dz \left[ \frac{d\sigma_{pp}^{\psi, dir, sing}}{dx_F} S_{\psi, dir, sing}^{abs}(b) \right.$$
$$+ \sum_{J=0}^{2} B(\chi_{cJ} \rightarrow \psi X) \frac{d\sigma_{pp}^{\chi_{cJ}, sing}}{dx_F} S_{\chi_{cJ}, sing}^{abs}(b)$$
$$+ \left. B(\psi' \rightarrow \psi X) \frac{d\sigma_{pp}^{\psi', sing}}{dx_F} S_{\psi', sing}^{abs}(b) \right]. \qquad (19)$$

In Ref. [43], the singlet cross section was assumed to be negligible. Therefore, $\sigma_{abs}^{oct} = 11$ mb was needed to produce an effective $\alpha$ equivalent to the assumption of pure octet production with $\sigma_{abs} = 7.3$ mb obtained in [11]. We use Eq. (17) and $\sigma_{\psi N}^s \neq 0$. Also, in Ref. [43], the authors only calculated the $x_F$-integrated cross sections. Here we use Eqs. (19) and (18) with the full $x_F$ dependence to calculate $\alpha(x_F)$ for $\psi$

and $\psi'$ absorption, shown in Fig. 5(c) at 800 GeV. The differences between the $\psi$ and $\psi'$ results arise from their distinct $x_F$ dependencies in the NRQCD model, predominantly from the $\chi_{cJ}$ contributions to $\psi$ production.

We have illustrated several different combinations of $\psi'$ and $\psi$ absorption cross sections in Fig. 5(c). We choose $\sigma_{\psi'N}^{\text{oct}} = \sigma_{\psi N}^{\text{oct}}$ as in pure octet production, Fig. 5(a), and $\sigma_{\psi'N}^{\text{sing}} \approx 3.7\sigma_{\psi N}^{\text{sing}}$, as in the pure singlet case shown in Fig. 5(b). The differences in $\alpha(x_F)$ for $\psi$ and $\psi'$ are small, especially between the solid and dashed curves with $\sigma_{\text{abs}}^{\text{oct}} = 1$ mb. The only obvious differences are at $x_F < 0$ when the $\psi'$ singlet contribution is larger and the $\psi'$ is still produced inside the target. However, at large $|x_F|$, $q\bar{q}$ annihilation, an octet contribution to $\psi'$, begins to become more important, causing the change in slope of $\alpha(x_F)$ here. This effect is not as strong for the $\psi$ because the $q\bar{q}$ contribution does not overtake the $gg$ until larger $x_F$. It is interesting to note that the effective $\alpha$ in the solid curve ($\sigma_{\text{abs}}^{\text{oct}} = 1$ mb and $\sigma_{\text{abs}}^{\text{sing}} = 1$ mb) is similar to the $\sigma_{\text{abs}}^{\text{o}} = 1$ result shown in Fig. 5(a) for pure octet absorption. Assuming a 3 mb octet absorption cross section results in a similar effective $\alpha$ at $x_F < 0$ in Figs. 5(a) and 5(c)—compare the dashed curve in 5(a) with the dot-dashed curve in 5(c). However, at forward $x_F$, the effective $\alpha$ in 5(c) is larger since the color singlet components escape without absorption, at least until the growing $q\bar{q}$ contribution causes the octet mechanism to dominate $\psi$ absorption once again at $x_F > 0.7$. The effect of singlet absorption would be even weaker at 120 GeV because the octet contributions make up a larger fraction of the production cross section at this energy.

The results with the absorption cross sections shown in Fig. 5 are only examples of the magnitude of the effects. It is clear, both from the data in Fig. 1 and from the initial state effects discussed in the following sections, that the model absorption cross sections must be smaller than those used previously when no initial state effects were included [10,11].

## V. HADRONIC COMOVERS IN $pA$ INTERACTIONS

Comoving secondaries, formed after $\tau_0 \sim 1-2$ fm, may also scatter with the $c\bar{c}$ pair or the $\psi$. Because $\tau_\psi \lesssim \tau_0$, the final-state charmonium is assumed to interact with the comovers. A spectator hadron moving with a velocity close to that of the charmonium state enhances the dissociation probability.

The $A$ dependence of $\psi$ production due to comovers alone is determined from

$$\sigma_{hA} = \sigma_{hN} \int d^2b [0.58 S_{\psi,\text{dir}}^{\text{co}}(b) + 0.3 S_{\chi_{cJ}}^{\text{co}}(b) + 0.12 S_{\psi'}^{\text{co}}(b)]. \tag{20}$$

The direct $\psi$-comover survival probability depends on the relative velocity of the $\psi$ and comovers, $v$, and the density of comovers at time $\tau$ and impact parameter $n(\tau,b)$ [15]. The initial density of the system can be related to the final hadron rapidity density [44]. In a $pA$ collision, the final-state multi-

plicity is $\approx \sigma_{hN} T_A(b) dN/dy$ where $dN/dy$ is the multiplicity in $pp$ interactions. The rapidity density grows with center-of-mass energy [45]. The shape of the produced particle rapidity density with inclusive $\psi$ production is unknown. We assume that the multiplicity slope is the same on both sides of midrapidity:

$$\frac{dN}{dy} = \frac{dN}{dy}\bigg|_{y=0} - ay, \tag{21}$$

where we take $dN/dy|_{y=0} = 1.07$ in $pp$ interactions at 800 GeV and $a = 0.108$ [45]. Since $\sigma_{hN}$ is approximately equal to the transverse area over which the comovers are produced, the direct $\psi$ survival probability in $hA$ collisions is [23]

$$S_{\psi,\text{dir}}^{\text{co}}(b) \approx \exp\left\{-\langle\sigma_{\psi\text{co}}v\rangle\frac{dN}{dy}\ln\left(\frac{\tau_I}{\tau_0}\right)T_A(b)\right\}, \tag{22}$$

where $\tau_I$ is the effective proper time the comovers interact with the $\psi$ and $\sigma_{\psi\text{co}}$ is the $\psi$-comover interaction cross section. The nuclear density profile is $T_A(b) = \int_{-\infty}^{\infty} dz\rho_A(b,z)$. The other survival probabilities for comover interactions with charmonium states are similar. We take $\sigma_{\psi\text{co}} = 0.67$ mb from a study of $\psi$ suppression in nucleus-nucleus data [10] with $\sigma_{\psi'\text{co}} \approx 3.7\sigma_{\psi\text{co}}$ and $\sigma_{\chi_{cJ}\text{co}} \approx 2.4\sigma_{\psi\text{co}}$ [42], assuming that the asymptotic charmonium states interact with the comovers.

The similarity between the survival probabilities in Eqs. (15) and (22) suggests that $\psi$-comover interactions do not introduce any unusual $A$ dependence. Thus comover contributions to $pA$ interactions, while small, are difficult to rule out entirely.

## VI. NUCLEAR SHADOWING

Measurements of the nuclear charged parton distributions by deep-inelastic scattering off both a large nuclear target and a deuterium target show that the ratio $R_{F_2} = F_2^A/F_2^D$ has a characteristic shape as a function of $x$ [12]. The region below $x \sim 0.1$ is referred to as the shadowing region and the range $0.3 < x < 0.7$ is known as the EMC region. In both regions, the parton density is depleted in the heavy nucleus relative to the deuteron, i.e., $R_{F_2} < 1$. At very low $x$, $x \approx 0.001$, $R_{F_2}$ appears to saturate [46]. Between the shadowing and EMC regions, an enhancement, antishadowing, is seen where $R_{F_2} > 1$. There is also an enhancement as $x \to 1$, assumed to be due to nucleonic Fermi motion. The general behavior of $R_{F_2}$ as a function of $x$ is often referred to as shadowing. Although this behavior is not well understood for all $x$, the shadowing effect can be modeled by an $A$ dependent fit to the nuclear deep-inelastic scattering data.

We have assumed that the nuclear parton distributions factorize into the nucleon parton distributions, independent of $A$, and a shadowing function that parametrizes the modifications of the nucleon parton densities in the nucleus, dependent on $A$, $x$, and $Q^2$:
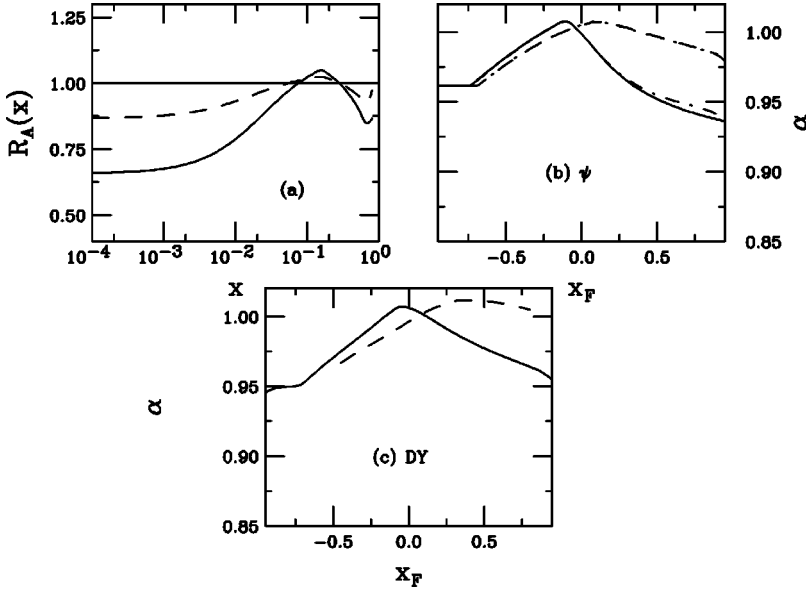
$$f_i^A(x,Q^2,A) = S^i(A,x,Q^2) f_i^p(x,Q^2).$$

FIG. 6. (a) The $S_1$ shadowing parametrization for W (solid) and Be (dashed) targets as a function of $x$. The resulting $A$ dependence for (b) $\psi$ production in the CEM and (c) Drell-Yan production is given at 800 GeV (solid) and 120 GeV (dashed). The NRQCD $\psi$ results are shown in (b) at 800 GeV (dot-dashed) and 120 GeV (dotted).

While the location of the parton in the target could influence $S^i$ [47], the impact parameter is difficult to resolve in $pA$ collisions. We use three different parametrizations of the shadowing function, $S^i(A,x,Q^2)$.

The first parametrization is a fit to nuclear deep-inelastic scattering data which does not differentiate between quark, antiquark, and gluon modifications and does not include evolution in $Q^2$. Therefore, it is not designed to conserve baryon number or momentum. We define $R_{F_2} = S_1(A,x)$ [48] with

$$
S_1(A,x) = \begin{cases}
R_s \dfrac{1+0.0134(1/x - 1/x_{\rm sh})}{1+0.0127A^{0.1}(1/x - 1/x_{\rm sh})} & x < x_{\rm sh} \\[2mm]
a_{\rm emc} - b_{\rm emc}x & x_{\rm sh} < x < x_{\rm Fermi} \\[2mm]
R_f \left( \dfrac{1 - x_{\rm Fermi}}{1-x} \right)^{0.321} & x_{\rm Fermi} < x < 1,
\end{cases}
\tag{23}
$$

where $R_s = a_{\rm emc} - b_{\rm emc}x_{\rm sh}$, $R_f = a_{\rm emc} - b_{\rm emc}x_{\rm Fermi}$, $b_{\rm emc} = 0.525(1 - A^{-1/3} - 1.145A^{-2/3} + 0.93A^{-1} + 0.88A^{-4/3} - 0.59A^{-5/3})$, and $a_{\rm emc} = 1 + b_{\rm emc}x_{\rm emc}$. The fit fixes the $x$ values at the boundaries of the $x$ regions, $x_{\rm sh} = 0.15$, $x_{\rm emc} = 0.275$, and $x_{\rm Fermi} = 0.742$. Thus, the nuclear parton distributions are modified so that

$$
f_i^A(x,Q^2) = S_1(A,x) f_i^p(x,Q^2).
\tag{24}
$$

The parametrization is available for all $A$ and is designed so that $S_1 \equiv 1$ when $A = 1$. Figure 6(a) shows the parametrization for $A = 184$ and $A = 9$. Note that the antishadowing region is rather narrow and saturation appears at $x < 10^{-3}$. Figures 6(b) and 6(c) give $\alpha(x_F)$ for $\psi$ and Drell-Yan production, respectively. Since this parametrization affects all partons equally, the results are independent of the chosen parton distribution function. They are also virtually independent of the charmonium production mechanism although there is a slight model dependence because the CEM involves an integral over $2m_c/\sqrt{s} < x < 2m_D/\sqrt{s}$, Eq. (7),

while in NRQCD $x_1$ and $x_2$ are either both fixed, e.g., when $C_{Q\bar{Q}[n]}^{ij} \propto \alpha_s^2$, or $x_1$ is fixed by the delta function in Eq. (8), while $4m_c^2/x_1 s < x_2 < 1$, when $C_{Q\bar{Q}[n]}^{ij} \propto \alpha_s^3$.

The second parametrization, $S_2^i(A,x,Q^2)$, modifies the valence quark, sea quark, and gluon distributions separately, and also includes $Q^2$ evolution [49], beginning at $Q = Q_0 = 2$ GeV and continuing up to $Q = 10$ GeV. It is based on a fit to the data using the Duke-Owens parton densities [50]. In this case, the nuclear parton densities are modified so that

$$
f_V^A(x,Q^2) = S_2^V(A,x,Q^2) f_V^p(x,Q^2),
\tag{25}
$$

$$
f_S^A(x,Q^2) = S_2^S(A,x,Q^2) f_S^p(x,Q^2),
\tag{26}
$$

$$
f_G^A(x,Q^2) = S_2^G(A,x,Q^2) f_G^p(x,Q^2),
\tag{27}
$$

where $f_V = u_V + d_V$ is the valence quark density and $f_S = 2(\bar{u} + \bar{d} + \bar{s})$ is the total sea quark density. It is assumed that $S_2^V$ and $S_2^S$ are the same for all valence and sea quarks, consistent with the symmetric sea of the Duke-Owens parton distributions. These modifications conserve baryon number, $\int_0^1 dx\, f_V^p(x,Q^2) = \int_0^1 dx\, f_V^A(x,Q^2)$, and the parton momentum sum, $\Sigma_P \int_0^1 dx\, x f_P^p(x,Q^2) = \Sigma_P \int_0^1 dx\, x f_P^A(x,Q^2)$ where $P = V$, $S$, and $G$, at all $Q^2$. Using parton densities other than Duke-Owens may lead to small deviations in the conservation rules.

The parametrization is only available for $A = 32$ and 200. It is thus applied only to the tungsten target and the beryllium densities are left unmodified. Figure 7(a) shows the ratios $S_2^V$, $S_2^S$, and $S_2^G$ at $Q = Q_0$ and $Q = 10$ GeV. At $Q_0$ the sea quarks are shadowed, more strongly at low $x$ than the gluons. Both the valence quarks and gluons are antishadowed while the sea quarks are not. The effects of evolution are weakest for the valence quarks and strongest for the gluons. Figures 7(b) and 7(c) show $\alpha(x_F)$ for $\psi$ and Drell-Yan production, respectively. The $\psi$ results in the CEM are given for the MRST LO [24] distributions and in the NRQCD ap-
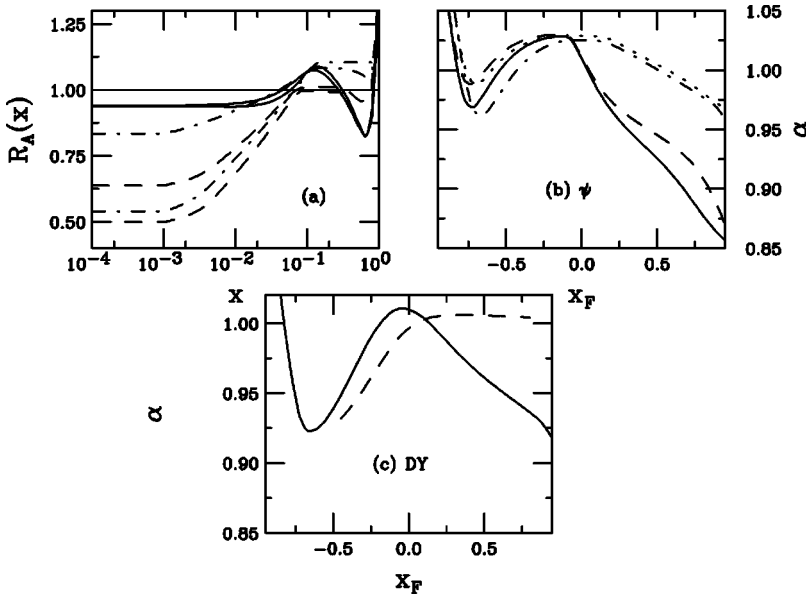
FIG. 7. (a) The $S_2$ shadowing parametrization for $A = 200$ as a function of $x$. The valence ratios, $R_V$, are given by the solid curves, the sea quark ratios, $R_S$, by the dashed curves, and the gluon ratios, $R_G$, are given by the dot-dashed curves. At small $x$, the lower curves are at $Q = 2$ GeV and the upper are at $Q = 10$ GeV. In (b) the $\psi$ $A$ dependence is illustrated for the CEM with MRST LO distributions at 800 GeV (solid) and 120 GeV (dot-dashed). The NRQCD results with the CTEQ $3L$ densities are also shown at 800 GeV (dashed) and 120 GeV (dotted). In (c) the Drell-Yan $A$ dependence is given for the MRST LO distributions at 800 GeV (solid) and 120 GeV (dashed).

proach with the CTEQ $3L$ [35] parton distributions. The main differences in the production models appear at negative $x_F$, corresponding to the EMC dip at large $x$ and appears because of the evolution of the gluon distributions at large $x$. The two calculations evolve differently because $m_c = 1.2$ GeV in the CEM and 1.5 GeV in NRQCD. The larger scale causes a smaller EMC dip in the shadowing ratio for the NRQCD calculation. The differences between production models at large $x_F$ are due in part to the $gq$ scattering contribution. Since this component is virtually negligible at 120 GeV, the model dependence is then small for $S_2$. Choosing other parton distribution functions for CEM $\psi$ and Drell-Yan production results in very similar ratios as for MRST LO.

A more recent shadowing parametrization, $S_3^i(A,x,Q^2)$, based on the GRV LO parton distributions [51], is now available [52,53]. The initial scale was chosen to equal the charm quark mass in the GRV LO distributions, $Q = Q_0 = 1.5$ GeV. At this scale all sea quark ratios are assumed to be equal, as

are both the valence ratios. The parameters are constrained by nuclear deep-inelastic scattering and Drell-Yan data. The gluon ratio is then fixed by the momentum sum rule as well as $\psi$ electroproduction data. Above $Q_0$, the individual quark and gluon distributions are evolved separately. The gluon distribution has a larger antishadowing peak in this parametrization, while the sea quarks are shadowed in the same region, a significant difference from $S_2$. The Drell-Yan data on the violation of the Gottfried sum rule [54] is taken to account, thus $S_3^{\bar{u}} \neq S_3^{\bar{d}}$ above $Q_0$. Evolution is taken up to $Q = 100$ GeV and the parametrization is generalized to all $A$, both improvements over $S_2$. Again, however, using other parton densities besides GRV LO could lead to small deviations from the conservation rules.

In Figs. 8(a) and 8(b), we show ratios for the $u_V$, $\bar{u}$, and $g$ densities at $Q = Q_0$ and 10 GeV for W and Be respectively. Figures 8(c) and 8(d) give the corresponding $\alpha(x_F)$ for $\psi$
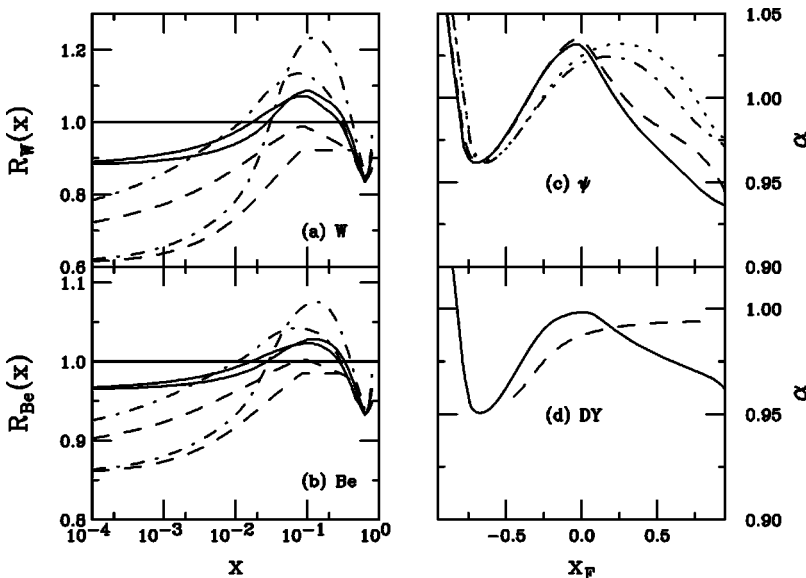


FIG. 8. The $S_3$ shadowing parametrization as a function of $x$ for (a) W and (b) Be targets. The valence up ratios, $R_{u_V}$, are given by the solid curves, the $\bar{u}$ ratios, $R_{\bar{u}}$, by the dashed curves and the gluon ratios, $R_G$, are given by the dot-dashed curves. At small $x$, the lower curves are at $Q = 1.5$ GeV, while the upper curves are at $Q = 10$ GeV. The resulting $A$ dependence for (c) $\psi$ and (d) Drell-Yan production is given. In (c) the $\psi$ $A$ dependence is illustrated for the CEM with MRST LO distributions at 800 GeV (solid) and 120 GeV (dot-dashed). The NRQCD results with the CTEQ $3L$ densities are also shown at 800 GeV (dashed) and 120 GeV (dotted). In (d) the Drell-Yan $A$ dependence is given for the MRST LO distributions at 800 GeV (solid) and 120 GeV (dashed).

and Drell-Yan production. The $\psi$ results in the CEM are given for the MRST LO distributions. Since gluon shadowing is not as strong as in the $S_2$ parametrization at low $x$, the effective $\alpha$ is larger at large $x_F$ than in Fig. 7(b). We have checked the CEM results with other parton distributions and found that the differences between the parton distributions are also more pronounced at large $x_F$ since the individual quark and antiquark distributions evolve separately, while with $S_2$, the valence and sea quarks, respectively, were considered together. In NRQCD, the effective $\alpha$ with the CTEQ $3L$ densities at 800 GeV is similar to the CEM results except at larger $x_F$ due to the $gq$ scattering contribution, as with the $S_2$ parametrization. However, at 120 GeV, the model dependence is more pronounced than with $S_2$, due to the larger relative importance of $q\bar{q}$ annihilation in the CEM than in NRQCD. This difference is again less important with the $S_2$ parametrization because it does not distinguish between the individual quark and antiquark distributions. At negative $x_F$ there is no difference due to evolution at the EMC dip because the ratios at large $x$ in Figs. 8(a) and 8(b) are essentially independent of $Q^2$. The Drell-Yan results are only shown for the MRST LO distributions. The reduced antiquark shadowing at low $x$ results in a larger $\alpha$ than with the $S_2$ parametrization.

To summarize, we note that the shape of $\alpha(x_F)$ is fixed by each parametrization. It is clear from the results in Figs. 6–8 that shadowing alone is insufficient to describe the preliminary E866 $\psi$ data as a function of $x_F$. This fact has been known for some time since the NA3 [3] and E772 [5] $\psi$ $A$ dependence was similar as a function of $x_F$ but not as a function of $x_2$ as would be expected if the nuclear dependence was dominated by shadowing.

## VII. EFFECTS OF ENERGY LOSS

Partons are expected to lose energy when traversing matter. This effect has been discussed primarily in the context of jet quenching [55,56]. Since the projectile parton is typically expected to feel the effects of energy loss, the scaling of the $A$ dependence at different energies with $x_F$ or $x_1$ suggested that energy loss could be the cause. We will introduce three models of energy loss that have been applied earlier to $\psi$ production and discuss their influence in the context of the E866 data.

### A. Initial state loss

Initial state energy loss, as studied by Gavin and Milana [13] and subsequently developed by Brodsky and Hoyer [14], takes a multiple scattering approach that essentially depletes the projectile parton momentum fraction, $x_1$, as the parton moves through the nucleus. Both the quarks and gluons can scatter elastically and lose energy before the hard scattering. This loss produces a similar effect for Drell-Yan and $\psi$ production. The motivation for this model stemmed from the fact that the $A$ dependence of $\psi$ production at 200 and 800 GeV seemed to scale with $x_F$ (or $x_1$) and not $x_2$ [3,5]. The projectile parton momentum fraction involved in the hard scattering is then $x_1' = x_1 - \Delta x_1$ where $x_1$ is the

original projectile parton momentum fraction when the parton first entered the target and $\Delta x_1$ represents the loss in $x_1$ due to multiple scatterings. Thus the shifted value, $x_1'$, enters the partonic cross sections but the parton distributions must be evaluated at the initial $x_1$. An additional delta function is added to Eqs. (4) and (8) with the corresponding integral over $x_1'$ so that Eq. (4) becomes

$$\frac{d\sigma^{c\bar{c}}}{dx_F dm^2} = \frac{1}{s}\int_0^1 dx_1' dx_1 dx_2$$

$$\times \delta(x_1' - x_1 + \Delta x_1)\delta(x_F - x_1' + x_2)$$

$$\times \delta(x_1' x_2 s - m^2)H_{AB}(x_1, x_1', x_2; m^2), \quad (28)$$

while Eq. (8) is then

$$\frac{d\sigma^C}{dx_F} = \sum_{i,j}\int_0^1 dx_1' dx_1 dx_2$$

$$\times \delta(x_1' - x_1 + \Delta x_1)\delta(x_F - x_1' + x_2)$$

$$\times f_i^A(x_1, \mu^2)f_j^B(x_2, \mu^2)\hat{\sigma}(ij \to C). \quad (29)$$

We first discuss the model by Gavin and Milana [13] and then the modifications suggested by Brodsky and Hoyer [14] with later refinements by Baier *et al.* [56].

The first model of initial-state energy loss applied to $J/\psi$ production was proposed by Gavin and Milana [13], referred to as GM hereafter. In their model, they assumed that

$$\Delta x_1 = \epsilon_i x_1 A^{1/3}\left(\frac{Q}{Q_0}\right)^{2n}, \quad (30)$$

with $n=1$. We do not include the $Q^2$ dependence in our calculations so that here $n=0$. The energy loss depends on the parton identity in this formulation. The initial $x_1$ is

$$x_1 = \frac{x_1'}{1 - \epsilon_i A^{1/3}}, \quad (31)$$

where $i=q$ or $g$ with $\epsilon_q = 0.00412$ and $\epsilon_g = 9\epsilon_q/4$ due to the difference in the color factors. When $n=0$, Eq. (30) corresponds to $-dE/dz|_q \sim 1.5$ GeV/fm and $-dE/dz|_g \sim 3.4$ GeV/fm [13]. In our calculations, we assume only initial state elastic scattering of the quarks and gluons. Final-state effects on the $\psi$ included in Ref. [13] are left out here under the assumption that final-state absorption provides a compensatory effect.

In Fig. 9 we show the results for this mechanism alone on the $A$ dependence of $\psi$ and Drell-Yan production. The $A$ dependence is weak at negative $x_F$ where $x_1$ is already small so that further reduction does not significantly change the quark and gluon distributions. This is true even for parton distributions that increase as $x_1^{-a}$ when $x_1$ is small and $a = 0.3-0.5$. As $x_F$ increases, $x_1$ grows larger and if the parton densities behave as $\sim(1-x_1)^{n_P}$ as $x_1 \to 1$, a slight decrease in $x_1$ is magnified. The effect should be stronger for $\psi$ than Drell-Yan production because $n_g \sim 5 > n_{q_V} \sim 3$ in simple
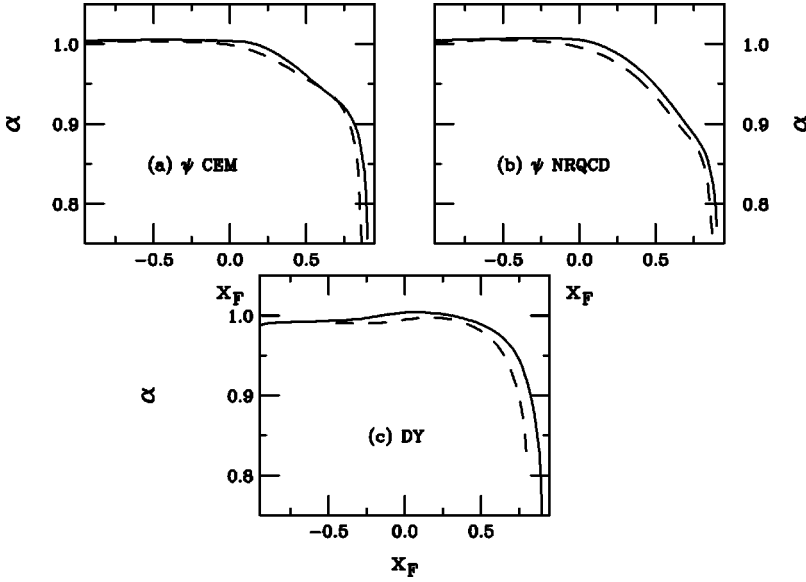
FIG. 9. The $A$ dependence assuming GM loss for $\psi$ production in (a) the CEM and in (b) NRQCD and (c) Drell-Yan production. In (a) the $\psi$ $A$ dependence is illustrated for the MRST LO distributions at 800 GeV (solid) and 120 GeV (dashed). The NRQCD results with CTEQ 3$L$ are shown in (b) at 800 GeV (solid) and 120 GeV (dashed). In (c) the Drell-Yan $A$ dependence is given for the MRST LO distributions at 800 GeV (solid) and 120 GeV (dashed).

spectator counting models [57] and the valence quark distributions are most important for Drell-Yan production at large $x_F$ (and $x_1$). The choice of parton densities does not change the shape of $\alpha(x_F)$. The energy dependence is also rather weak. A comparison of Figs. 9(a) and 9(b) shows that the behavior of $\alpha(x_F)$ does not depend strongly on the $\psi$ production model although there is evidence that the effect begins to be non-negligible at a lower $x_F$ in the NRQCD approach.

Later, Brodsky, and Hoyer [14] (BH) argued that the energy loss in the Gavin and Milana model was too large because there is not enough time after the initial QCD bremsstrahlung for the color field of the parton to be regenerated. Therefore, the subsequent interactions of the parton in the target do not lead to a large increase in energy loss [58]. From the uncertainty principle they deduced that the loss should be independent of parton type and the change in $\Delta x_1$ should be bound so that

$$\Delta x_1 < \frac{\langle k_\perp^2 \rangle L_A}{2E}, \tag{32}$$

where $L_A$ is the path length through the medium and $\langle k_\perp^2 \rangle$ is the average transverse momentum of gluons radiated by the incoming parton. If $E = x_1 s / 2m_p$ and $L_A \sim R_A \propto A^{1/3}$, then

$$\Delta x_1 \lesssim \frac{\kappa}{x_1 s} A^{1/3}, \tag{33}$$

where $\kappa \propto m_p \langle k_\perp^2 \rangle$. The average radiative loss is thus expected to be $-dE/dz \sim 0.25$ GeV/fm with another 0.25 GeV/fm loss expected to arise from elastic scattering. In this case, when $\Delta x_1 \propto c / x_1$, $x_1 = 0.5(x_1' + \sqrt{(x_1')^2 + 4c})$. The $x_F$ dependence of $\alpha$ when $c = \kappa A^{1/3} / s$, referred to henceforth as ''original BH loss,'' is given by the dotted and dot-dash-dashed curves in Fig. 10 for $\psi$ and Drell-Yan production.
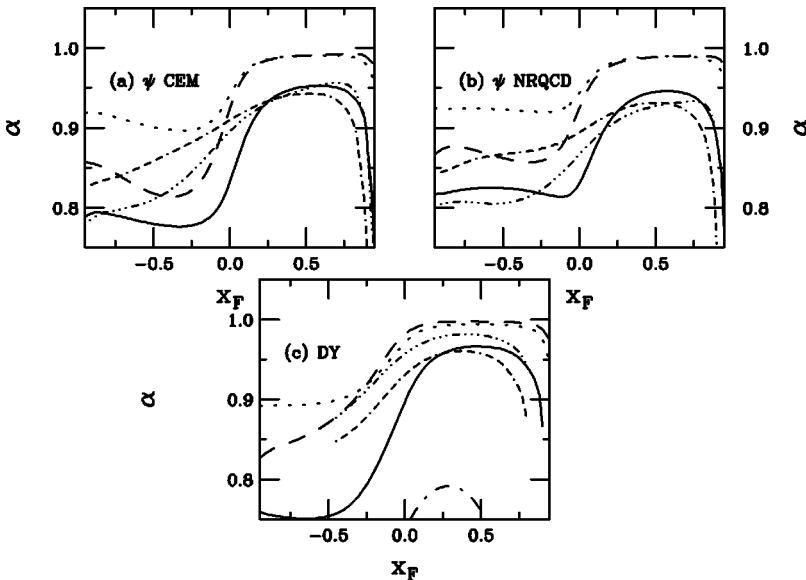


FIG. 10. The $A$ dependence assuming BH loss for $\psi$ in (a) the CEM and in (b) NRQCD, and (c) Drell-Yan production. The MRST LO distributions are used for CEM $\psi$ and Drell-Yan production, while CTEQ 3$L$ densities are used with NRQCD $\psi$ production. The maximum BH loss [Eq. (37)], is shown in the solid curves at 800 GeV and in the dot-dashed curves at 120 GeV. The minimum BH loss [Eqs. (38) and (39)], is shown in the dashed curves at 800 GeV and in the dot-dot-dot-dashed curves at 120 GeV. The original BH loss [Eq. (33)], is shown in the dotted curves at 800 GeV and in the dot-dash-dash-dashed curves at 120 GeV.

Subsequently, the bound on $dE/dz$ was refined through the work of Baier *et al.* [56,59] where they determined

$$-\frac{dE}{dz} = \frac{3\alpha_s}{4}\langle p_{\perp W}^2 \rangle, \tag{34}$$

with $\langle p_{\perp W}^2 \rangle$ the characteristic squared transverse momentum of the parton.[3] The value of the radiative loss is independent of the details of the scattering process as long as $L_A$ is large. In this description, $\Delta x_1$ is then

$$\Delta x_1 = \frac{3\alpha_s}{2}\frac{m_p}{x_1 s}L_A\langle p_{\perp W}^2 \rangle, \tag{35}$$

where the average transverse momentum $\langle p_{\perp W}^2 \rangle$ is proportional to $A^{1/3}$ [56]. Since $\langle p_{\perp W}^2 \rangle \propto A^{1/3}, \Delta x_1 \propto A^{2/3}$ in Eq. (35) rather than $A^{1/3}$ as postulated by Brodsky and Hoyer [14] [Eq. (33)] because they assumed that $\langle k_\perp^2 \rangle$ was independent of $A$.

Two estimates of $\langle p_{\perp W}^2 \rangle$ were provided in Ref. [56]. The larger value, used as an upper limit, comes from a single nuclear rescattering of photoproduced dijets [61],

$$\langle p_{\perp W}^2 \rangle = \pi^2 \alpha_s \lambda_{LQS}^2 A^{1/3} \frac{C_A \sigma_g^{\gamma A} + C_F \sigma_q^{\gamma A}}{\sigma^{\gamma A}}. \tag{36}$$

They obtained $0.05 < \lambda_{LQS}^2 < 0.1$ GeV$^2$ by assuming that dijet production is dominated either by quarks or gluons using the measured $p_T$ broadening as a function of $A$. With the lower bound on $\lambda_{LQS}^2$,

$$\langle p_{\perp W}^2 \rangle \simeq 0.658 \alpha_s A^{1/3} \ \text{GeV}^2. \tag{37}$$

Since the initial states could not be explicitly identified, we assume that $\langle p_{\perp W}^2 \rangle$ is identical for quarks and gluons. Then when $\alpha_s \sim 0.3$ and $A = 184$, we find $-dE/dz \simeq 1.28$ GeV/fm with Eq. (37). We refer to this as ''maximum BH loss'' in the remainder of the discussion even though $dE/dz$ is actually smaller than the proposed GM loss. [The difference in the subsequent shapes of $\alpha(x_F)$ lies in the form of $\Delta x_1$.] The second estimate depends on the nucleon gluon distribution and contains explicit color factors so that

$$\langle p_{\perp W}^2 \rangle_q = \frac{2\pi^2 \alpha_s}{3}\rho_A x G(x,Q^2)L_A \simeq 0.07\alpha_s A^{1/3} \ \text{GeV}^2, \tag{38}$$

$$\langle p_{\perp W}^2 \rangle_g = \frac{9}{4}\langle p_{\perp W}^2 \rangle_q \simeq 0.15\alpha_s A^{1/3} \ \text{GeV}^2, \tag{39}$$

where $xG(x) \sim 1-2$ for the $x_1$ range of E866. This lower estimate is referred to subsequently as ''minimum BH loss.''

---

[3] After the inclusion of other diagrams suggested by Zakharov [60], Baier *et al.* concluded that the loss derived in Ref. [56] was, in fact, a factor of two larger [59]. This difference is reflected in Eq. (34).

Now when $\alpha_s \sim 0.3$ and $A = 184$, $-dE_q/dz \simeq 0.12$ GeV/fm and $-dE_g/dz \simeq 0.28$ GeV/fm.

The resulting $x_F$ dependence of $\alpha$ is shown in Fig. 10 at 800 and 120 GeV. At negative $x_F$, $x_1$ can be considerably larger than $x_1'$, up to an order of magnitude as $x_F \to -1$ at 800 GeV. The difference in shapes at negative $x_F$ between the CEM and NRQCD arise from the relative importance of $q\bar{q}$ annihilation and $gg$ fusion (as well as $qg$ scattering in NRQCD). Even though the energy loss is the same for quarks and gluons with the original and maximum BH loss estimates, the relative change is larger for the gluon than the sea quark distributions when $x_1$ is small. At large negative $x_F$, the $q\bar{q}$ contribution is dominant with $\Sigma_q q(x_1)\bar{q}(x_2) \approx \bar{u}(x_1)u(x_2) + \bar{d}(x_1)d(x_2)$ and the change in the projectile sea quark distribution is less than that of the gluon distribution. When $gg$ fusion dominates, $\alpha(x_F)$ decreases. In the NRQCD model, the $qg$ contribution tends to balance this difference, leading to the flatter $\alpha(x_F)$ for $x_F < 0$, particularly at 800 GeV. As $x_F$ approaches zero, the change in all the distributions becomes smaller. The change in $x_1$ due to the minimum BH loss is only $\sim 20\%$ at $x_F \approx 0$, decreasing to less than 8% at $x_F = 0.1$. Note also that the predicted minimum loss for gluons, Eq. (39), and the original BH loss [Eq. (33)] result in a similar $\alpha(x_F)$ at forward $x_F$ even though the $A$ dependencies of the two are different. That is because the shift in $x_1$ is reduced at large $x_F$, the change in all parton densities is small when $x_1 \approx 0.1-0.9$ and the original BH model $dE/dz$ is very similar to $dE_g/dz$ for the minimum BH loss. At 800 GeV, the drop at large $x_F$ is due to loss by valence quarks since at large $x_F$, $\Sigma_q q(x_1)\bar{q}(x_2) \approx \bar{u}(x_2)u(x_1) + \bar{d}(x_2)d(x_1)$. At 120 GeV, the effect of the loss is larger since $\Delta x_1 \propto 1/s$. The correspondingly higher $x_1'$ values at 120 GeV reduce the gluon distribution shift relative to $q\bar{q}$. This, as well as the greater importance of $q\bar{q}$ annihilation, results in the different shapes of $\alpha(x_F)$ for the two energies at negative $x_F$.

The Drell-Yan results are similar to the calculated $\psi$ results except that the Drell-Yan loss is weaker at larger $x_F$. Part of the difference is because $x_1$ and the scale $M$ at which the parton densities are evaluated are both greater than for the $\psi$. We can also see that the maximum BH loss is almost certainly too large to explain the current Drell-Yan results. Indeed, at 120 GeV, $\alpha(x_F)$ barely appears on the plot. The Drell-Yan results are similar to the calculated $\psi$ results except

The large change in $x_1$, appearing as large $\Delta x_1$, suggests that the calculation may not be applicable for $\Delta x_1 > x_1$. At 800 GeV, $\Delta x_1 = x_1$ occurs when $0.03 \leq x_1 \leq 0.09$, depending on the loss estimate, corresponding to a minimum $x_F$ of $-0.1 \leq x_F \leq 0.02$. At 120 GeV, the $x_1$ values are larger, $x_1 \approx 0.1-0.3$ for the original and minimum BH loss estimates and 0.6 for the maximum BH estimate, corresponding to $x_F \approx -0.2-0$ and 0.5, respectively. In our calculations, we will apply the model over all $x_F$.

We finally note that neither of these initial state models of energy loss alone can reproduce the data. GM loss does not

have the same curvature of the data at large $x_F$ while BH loss is too weak at large $x_F$ and too strong at low $x_F$.

### B. Final state loss

The second model of energy loss we consider is applicable only to the quarkonium system and not to Drell-Yan production which does not involve color confinement in the final state [17]. When a $c\bar{c}$ pair is produced in a color octet state, it has to emit a soft gluon in order to produce the final-state $\psi$ or $\psi'$. This $c\bar{c}$ can propagate some distance, essentially longer than its path through the nucleus, before the soft gluon is finally emitted. This is because the Landau-Pomeranchuk-Migdal effect [58] in QCD causes a delay in the emission of the third gluon to neutralize the color of the $c\bar{c}$ state due to successive interactions of the colored $c\bar{c}$ pair in the medium. However, each successive interaction of the $c\bar{c}$ pair degrades its momentum.

This final-state loss model, developed by Kharzeev and Satz [17] and referred to as KS loss here, is applicable only when the $c\bar{c}$ pair interacts in the color octet state, essentially for $x_F \gtrsim 0$. After $n$ interactions along its path length before leaving the target, the pair's momentum is reduced by $\sim \kappa L_A$ where $\kappa$, the hadronic string tension, is determined from lattice studies of confinement between colored objects, $\kappa \sim (9/4)$ GeV/fm [17], and $L_A$ is the distance the pair has traveled through the target, calculated for the nuclear shape distributions in Ref. [38]. A $\psi$ state observed at a given $x_F$ has actually been produced with a higher value, $x_F/\delta$, where $\delta \approx 1 - \kappa L_A / P_\psi$ and $P_\psi$ is the $\psi$ momentum in the center-of-mass frame.

The $x_F$ distribution $G_A(x_F)$ then has two parts [17],

$$G_A(x_F) \propto S_A G_p(x_F) + (1 - S_A) \frac{G_p(x_F/\delta)}{\delta} \theta(1 - x_F/\delta),$$
(40)

where $G_p(x_F)$ is the $x_F$ distribution in $pp$ interactions and $S_A$ is the survival probability for the $c\bar{c}$ pair not to break up on its way out of the target, calculated in Eq. (15) for pure octet production. The second term includes the scatterings in the target that cause the shift in $x_F$. The effect of Eq. (40) does not produce an integrated $\psi$ suppression, the integrated $\alpha$ in Eq. (1) is unchanged with this mechanism, only $\alpha(x_F)$ changes due to the shift in $x_F$.

The resulting $x_F$ dependence is shown in Fig. 11 for $x_F \geq 0$. We have illustrated the effect for the MRST LO parton densities at 800 GeV with three different color octet cross sections: 1, 20, and 40 mb. A 20 mb cross section was chosen originally [17] to be as large as a typical meson-nucleon inelastic cross section at the same energy, $\sigma_{abs} \approx \sigma_{\pi N}^{inel} \approx 20$ mb. The 1 mb cross section shows a minimal effect, while $\sigma_{abs} \approx 40$ mb sets the scale for the maximum effect since then $\sigma_{abs} > \sigma_{pp}^{inel}$. While a large octet cross section is needed to produce a strong effect at $x_F > 0.5$, the normalization amplifies $\alpha(x_F \sim 0)$ so that the shape of the dependence is significantly different from the behavior of the E866 data at low $x_F$. Including shadowing will further increase $\alpha$ for $x_F \sim 0$,
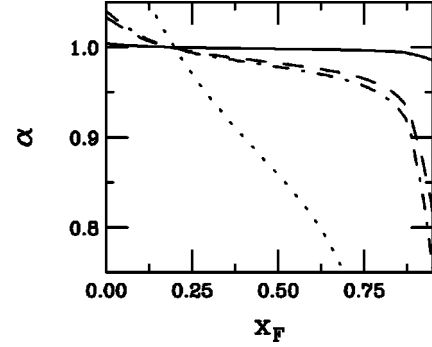


FIG. 11. The $A$ dependence of $\psi$ production assuming KS loss for $x_F > 0$. Octet cross sections of 1 mb (solid), 20 mb (dashed), and 40 mb (dot-dashed) are calculated with the MRST LO parton densities at 800 GeV. At 120 GeV, a 40 mb octet cross section is assumed (dotted).

as we will see. Due to its nature, this model is limited to the case where all $\psi$'s are assumed to be produced in pure color octet states.

It is clear that KS loss alone cannot account for the shape of the $\psi$ and $\psi'$ data in Fig. 1. A combination of effects is needed.

### VIII. INTRINSIC CHARM

The wave function of a proton in QCD can be represented as a superposition of Fock state fluctuations, e.g., $|uudg\rangle$, $|uudq\bar{q}\rangle$, $|uudQ\bar{Q}\rangle$, ... of the $|uud\rangle$ state. When the projectile scatters in the target, the coherence of the Fock components is broken and the fluctuations can hadronize [18,62]. These intrinsic $Q\bar{Q}$ Fock states are dominated by configurations with equal rapidity constituents so that, unlike sea quarks generated from a single parton, the intrinsic heavy quarks carry a large fraction of the parent momentum [18].

The frame-independent probability distribution of a five-particle $c\bar{c}$ Fock state in the proton is

$$\frac{dP_{ic}^5}{dx_i \cdots dx_5} = N_5 \alpha_s^4(m) \frac{\delta\left(1 - \sum_{i=1}^5 x_i\right)}{\left(m_p^2 - \sum_{i=1}^5 (\hat{m}_i^2/x_i)\right)^2},$$
(41)

where $N_5$ normalizes the $|uudc\bar{c}\rangle$ probability, $P_{ic}^5$. The delta function conserves longitudinal momentum. The denominator is minimized when the heaviest constituents carry the largest fraction of the longitudinal momentum, $\langle x_Q \rangle > \langle x_q \rangle$, maximizing $P_{ic}^5$. We choose $\hat{m}_q = 0.45$ GeV and $\hat{m}_c = 1.8$ GeV [20].

The intrinsic charm production cross section from the five-particle state can be related to $P_{ic}^5$ and the inelastic $pN$ cross section by

$$\sigma_{ic}^5(pN) = P_{ic}^5 \sigma_{pN}^{in} \frac{\mu^2}{4\hat{m}_c^2}.$$
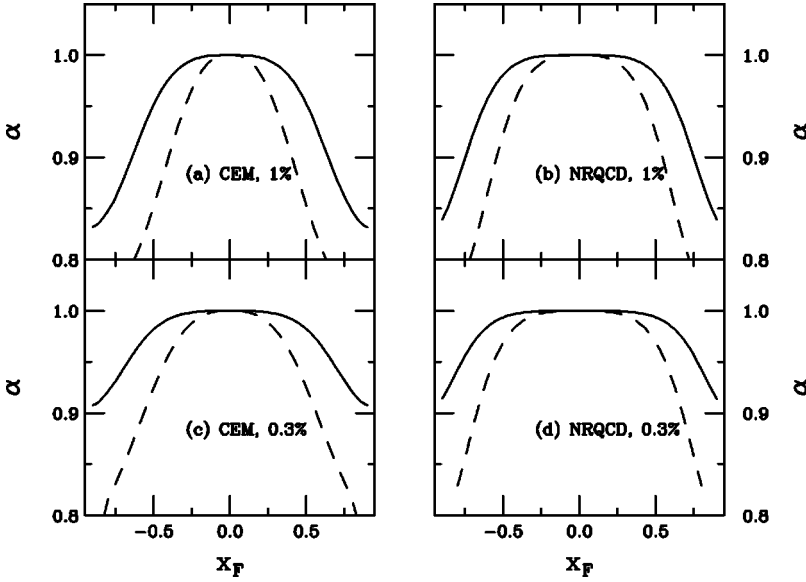(42)

FIG. 12. The $A$ dependence of intrinsic charm at 800 GeV (solid) and 120 GeV (dashed). In (a) and (c) an effective production probability of 1% is assumed in the CEM and in NRQCD, respectively, while in (c) and (d) $P_{ic}^{eff}=0.31\%$ is assumed in the CEM and in NRQCD.

The factor of $\mu^2/4\hat{m}_c^2$ arises from the soft interaction which breaks the coherence of the Fock state. We assume that the NA3 diffractive $\psi$ cross section [3], the second term in Eq. (2) proportional to $A^\beta$, can be attributed to intrinsic charm and find $\mu^2 \sim 0.1$ GeV$^2$.

While the total intrinsic charm cross section is relatively easy to define, there are some uncertainties in the relative weights of open charm and $\psi$ production from an intrinsic charm state. In general, the $\psi$ production cross section is significantly smaller than the open charm production cross section. There are several factors that can suppress $\psi$ production relative to open charm in standard charmonium production models, such as the CEM and NRQCD, as well as in the intrinsic charm model. As in the CEM, the probability to produce a $\psi$ from an intrinsic $c\bar{c}$ state is proportional to the fraction of intrinsic $c\bar{c}$ production below the $D\bar{D}$ threshold. The fraction of $c\bar{c}$ pairs with $2m_c < m < 2m_D$ is

$$f_{c\bar{c}/h} = \int_{4m_c^2}^{4m_D^2} dm^2 \frac{dP_{ic}}{dm^2} \Bigg/ \int_{4m_c^2}^{s} dm^2 \frac{dP_{ic}}{dm^2}, \qquad (43)$$

typically smaller than that obtained in the CEM [21]. However, as discussed in Sec. II A, not all $c\bar{c}$ pairs below the $D\bar{D}$ threshold will produce a final state $\psi$. The fraction that actually become $\psi$'s is rather small, on the order of 2.5% in the CEM [21]. Since the additional suppression factors involved in the intrinsic charm model are not completely fixed [63], rather than discuss all the uncertainties here, we will use an effective intrinsic charm probability, $P_{ic}^{eff}$. The EMC charm structure function data is consistent with $P_{ic}^5 = 0.31\%$ for low energy virtual photons but $P_{ic}^5$ could be as large as 1% for the highest virtual photon energies [64,65]. Typically the more conservative result is used but in this paper, we will use the larger value in most of our calculations and show the effect of reducing and/or eliminating the intrinsic charm component.

Including a delta function to combine the $x_c$ and $x_{\bar{c}}$ in the $\psi$ state, the $\psi x_F$ distribution from intrinsic charm is

$$\frac{d\sigma_d}{dx_F} = \sigma_{pN}^{in} \frac{\mu^2}{4\hat{m}_c^2} \int \prod_{i=1}^{5} dx_i \frac{dP_{ic}^{eff}}{dx_1 \ldots dx_5} \delta(x_F - x_c - x_{\bar{c}}). \tag{44}$$

Only the five-particle Fock state is considered. The intrinsic charm contribution is included as in Eq. (2) with $\beta=0.71$. The total $A$ dependence for intrinsic charm alone is shown in Fig. 12 assuming $P_{ic}^{eff}=1\%$ and 0.31% with both charmonium production models. The contribution is symmetric around $x_F=0$ since the projectile and target fragmentation regions are treated equally. Figures 12(a) and 12(c) show $\alpha(x_F)$ in the CEM. A larger effect is seen at high $x_F$ with the NRQCD model, Fig. 12(b), because the NRQCD $x_F$ distribution is narrower. Since charmonium production models outlined in Sec. II have a larger energy dependence than the intrinsic charm cross section in Eq. (42), intrinsic charm is more important at 120 GeV. When $P_{ic}^{eff}=0.31\%$, the intrinsic charm contribution to the total $A$ dependence is quite small and only significant for the largest $x_F$ values due to the reduced $A$ dependence of the mechanism. Assuming a 1% probability enhances the intrinsic charm effect at large $x_F$ and even suggests that intrinsic charm can influence $\alpha(x_F)$ at $x_F \sim 0$.

## IX. RESULTS AND PREDICTIONS

We now have a comprehensive model with which we can confront the nuclear dependence of $\psi$, $\psi'$, and Drell-Yan production. The nuclear effects included in the model are shadowing of the parton distributions, energy loss, nuclear absorption, comover interactions, and the ''diffractive'' intrinsic charm component. It is clear from an examination of the individual nuclear effects shown in Figs. 5–12 that no single mechanism can correctly predict the shape of the E866 $x_F$ data.

TABLE I. The $\psi$ absorption cross sections used with each shadowing parametrization. Note that the corresponding $\psi'$ absorption cross sections are the same as those for the $\psi$ in the octet case and a factor of 3.7 larger for singlet production. In all cases the comover cross sections are $\sigma_{\psi\text{co}}=0.67$ mb and $\sigma_{\psi'\text{co}}=3.7\sigma_{\psi\text{co}}$.

|  | Octet $\sigma_{\psi N}^{o}$ (mb) | Singlet $\sigma_{\psi N}^{s}$ (mb) | Combination $\sigma_{\psi N}^{\text{oct}}$ (mb) | $\sigma_{\psi N}^{\text{sing}}$ (mb) |
|---|---|---|---|---|
| $S_1$ | 2 | 8 | 3 | 2 |
| $S_2$ | 1 | 5 | 1 | 1 |
| $S_3$ | 3 | 10 | 3 | 5 |

To compare with the preliminary data, we calculate $\alpha(x_F)$ of $\psi$ and $\psi'$ production with all three models of energy loss and all shadowing parametrizations. For pure octet absorption, we use all three models of energy loss. Only GM and BH loss are used with pure singlet absorption and the combination of singlet and octet production. The CEM model with the MRST LO parton distributions is used to calculate charmonium production for pure octet and pure singlet absorption. NRQCD is used as the basic production model for the octet/singlet combination, Eq. (19). All three shadowing parametrizations are used in each case. We use an effective intrinsic charm probability of 1% but will examine the relative importance of intrinsic charm to the overall description of the large $x_F$ E866 data. The absorption cross sections are chosen so that the shadowing parametrization gives reasonable agreement with the magnitude of $\alpha(x_F)$ for both $\psi$ and $\psi'$ production at $x_F>0$ with GM loss. We do not actually make detailed fits to the data to obtain the cross sections. The resulting absorption cross sections are given in Table I for GM and BH loss. The KS model of energy loss is always calculated with an octet absorption cross section of 40 mb. The NA3 Pt/$^2$H ratio as a function of $x_F$ at 200 GeV is also compared to the model calculations. We make predictions of the $\psi$ and $\psi'$ $A$ dependence at 120 GeV. Finally, we show

the combined effects of shadowing and initial-state energy loss on Drell-Yan production at 800 and 120 GeV.

In this work, we assume that shadowing and energy loss effects are independent. This assumption depends on the ultimate source of nuclear shadowing because the mechanism of GM and BH energy loss is multiple parton scattering before the hard collision. If shadowing in deep-inelastic scattering is due to the recombination of high density partons, no rescattering is involved and the effects are independent. If shadowing is caused by $\gamma^{\star}\rightarrow q\bar{q}$ with the $q\bar{q}$ pair free to rescatter as a vector meson, the origin of the two effects is similar. The vector-meson approach is a low $Q^2$ effect, lower than the effective $Q^2$ needed for $\psi$ production. Therefore, we assume that the two effects are independent and include both in our calculations.

We first compare our full model results with the preliminary E866 $\psi$ data in Figs. 13, 14, and 15. Each figure shows the difference in the shadowing mechanisms for each type of energy loss with a particular absorption mechanism. In Fig. 13, the pure octet absorption mechanism is shown. The results with GM loss, Fig. 13(a), best reproduce the general trend of the data for $x_F>0.1$. In general the agreement is worse at $x_F<0$ because $x_2$ is in the antishadowing region where antishadowing of gluons enhances $\alpha(x_F)$, see Figs. 6–8. The KS loss model is typically above the data, except for the $S_2$ parametrization, and is inconsistent with the shape of the preliminary E866 data at $x_F<0.2$. Since the KS model is only applicable for $x_F\geq0$, we make no further calculations with this model. The calculations of $\alpha(x_F)$ with BH loss [Figs. 13(c)–13(e)], do not match the data very well at low $x_F$, particularly for the maximum BH loss. While the results with the maximum loss [Eq. (37)] produce the largest reduction at large $x_F$, the negative $x_F$ region is far off due to the drop in $\alpha$ at negative $x_F$. The curvature of $\alpha(x_F)$ changes at $x_F\sim0.1-0.25$, the point at which the slope of the BH loss flattens in Fig. 10(a). Better results are achieved with the
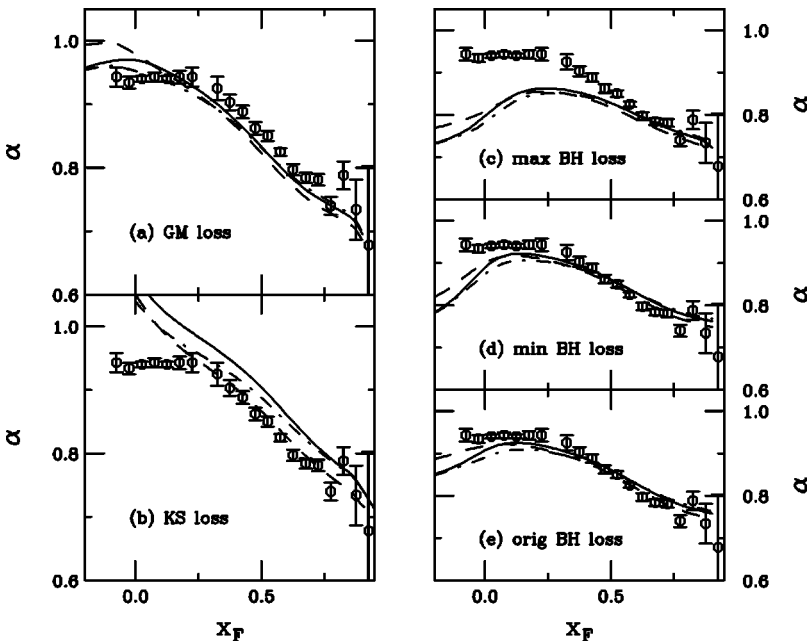


FIG. 13. All effects are compared with the preliminary E866 $\psi$ data [9] assuming pure octet absorption. In (a) and (b), GM and KS loss are assumed. Energy loss effects associated with the BH bound are shown in (c), (d), and (e) for the estimated maximum and minimum loss and the original bound, respectively. All calculations are in the CEM with the MRST LO parton densities. The curves represent shadowing with the $S_3$ (solid), $S_2$ (dashed), and $S_1$ (dot-dashed) parametrizations.
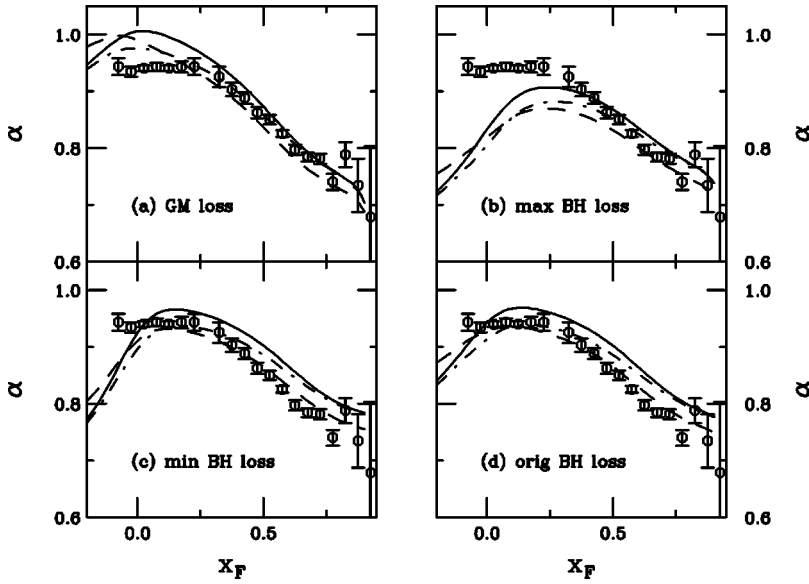
FIG. 14. All effects are compared with the preliminary E866 $\psi$ data [9] assuming pure singlet absorption. In (a), GM loss is assumed. Energy loss effects associated with the BH bound are shown in (b), (c), and (d) for the estimated maximum and minimum loss and the original bound, respectively. All calculations are in the CEM with the MRST LO parton densities. The curves represent shadowing with the $S_3$ (solid), $S_2$ (dashed), and $S_1$ (dot-dashed) parametrizations.

lower estimates of the BH loss, the minimum estimate [Eqs. (38) and (39)], and the original suggestion [Eq. (33)]. The data are somewhat overestimated at $x_F < 0.2$ with the minimum loss but the overestimate is slight for the original BH loss with the $A^{1/3}$ dependence. Choosing a smaller absorption cross section would improve the agreement with the data at low $x_F$ although it would worsen the agreement at $x_F > 0.25$. We also note that none of the absorption cross sections are greater than 3 mb, already more than a factor of 2 less than the 7.3 mb effective absorption cross section found in Ref. [11].

Pure singlet absorption, shown in Fig. 14, results in somewhat poorer agreement with the data than pure octet absorption because the $\psi$ is always produced outside the target when $x_F > 0$ at 800 GeV. Therefore, changing the absorption cross section would not improve the agreement with the data. The choice of parton distribution function in the CEM results in small changes in the shape of $\alpha(x_F)$ and does not influence the overall agreement with the data.

A combination of octet and singlet absorption in the NRQCD $\psi$ production model produces rather good agreement for all shadowing parametrizations when the GM model is applied, Fig. 15(a). The difference in curvature at $x_F > 0$ between the calculations with BH loss and the preliminary data are larger than in the CEM because the $A$ dependence of shadowing in NRQCD is weaker at positive $x_F$ than that of the CEM, see Figs. 6–8. As explained in Sec. VI, the difference in the $A$ dependence of the two production models is due to the chosen $x$ values and the charm quark mass which sets the scale for evolution.

In all cases, the most striking disagreement of the GM loss model with the data occurs at $x_F < 0.1$ when the calculated $\alpha$ slightly overshoots the data due to the antishadowing of the gluon distribution. The shape of $\alpha(x_F)$ here depends most strongly on the shadowing parametrization since the other $x_F$ dependent contributions are rather slowly varying. None of these parametrizations produce the same curvature as the data and, even if they did, the additional absorption
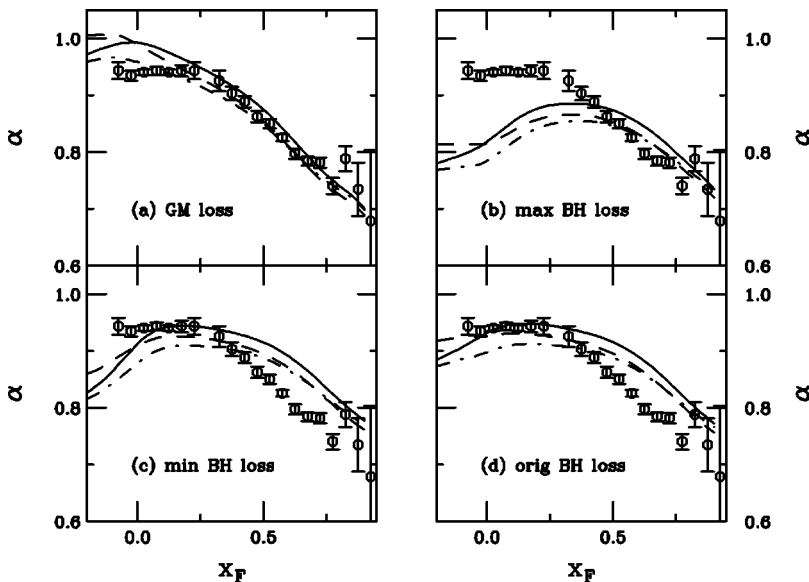


FIG. 15. All effects are compared with the preliminary E866 $\psi$ data [9] assuming a combination of octet and singlet production and absorption. In (a), GM loss is assumed. Energy loss effects associated with the BH bound are shown in (b), (c), and (d) for the estimated maximum and minimum loss and the original bound, respectively. All calculations are in NRQCD with the CTEQ 3$L$ parton densities. The curves represent shadowing with the $S_3$ (solid), $S_2$ (dashed), and $S_1$ (dot-dashed) parametrizations.
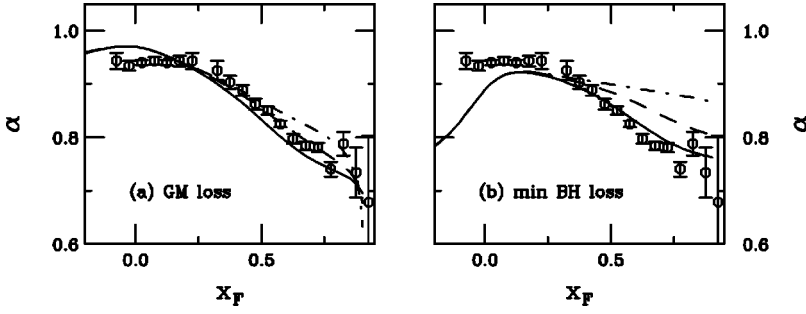
FIG. 16. The effective probability of intrinsic charm is varied for pure octet production with (a) GM loss and (b) the minimum BH loss. The curves represent an effective intrinsic charm probability of 1% (solid), 0.31% (dashed), and 0% (dot-dashed).

required for the calculations to agree with the data would ruin the agreement of the model with the data at forward $x_F$. Increasing absorption at $x_F < 0$ by artificially enhancing the comover density would not significantly improve the agreement.

The pure octet and pure singlet calculations with BH loss are in reasonably good agreement with the data for $x_F > 0.2$. The maximum estimated loss is in clear disagreement with the data at all $x_F$, both in shape and in magnitude. This disagreement would persist, even if final-state absorption of the $\psi$ were ignored.[4] It is also then unlikely to produce results consistent with the minimal $A$ dependence of Drell-Yan production, especially at lower energies, as we discuss later. The agreement with the minimum and original BH calculations is reasonable for $x_F > 0.2$. At lower $x_F$ values, the change in $\Delta x_1$ due to the energy loss is large. However, since $\Delta x_1 \sim x_1$ at $x_F \sim 0$, the model is at the limit of applicability and therefore the magnitude of the disagreement is suspect.

To show the influence of intrinsic charm, we take the $S_3$ shadowing parametrization with GM and minimum BH loss and vary $P_{ic}^{eff}$ between 0 and 1% in Fig. 16. We choose pure octet production and absorption because the agreement with the data seems to be among the best [see Figs. 13–15]. Since the GM loss mechanism alone causes strong reduction in $\alpha$ at large $x_F$ [see Fig. 9], including intrinsic charm does not have a large effect. It would appear from Fig. 16(a) that $P_{ic}^{eff} = 0.31\%$ agrees best with the data although the agreement is reasonable in all three cases. The same is true for the combination model but pure singlet absorption would require a larger intrinsic charm probability to agree with the data. On the other hand, the relatively good agreement of the minimum BH loss calculations with the data at large $x_F$ is due to the intrinsic charm contribution. Without intrinsic charm with $P_{ic}^{eff} = 1\%$, the model calculations would not agree with the data. The minimum and original BH loss models affect $\alpha$ weakly at positive $x_F$ and shadowing alone can only reduce $\alpha$ to $\sim 0.85$ as $x_F \rightarrow 1$ with the $S_2$ parametrization [see Fig. 7]. Thus increasing the relative intrinsic charm contribution is the only way to produce agreement with the data at large $x_F$. This is clearly shown in Fig. 16(b). With no intrinsic charm, $\alpha(x_F)$ is relatively flat at large $x_F$. Similar results are

obtained with the pure singlet and combination absorption models. Note that for both loss mechanisms, intrinsic charm only affects the shape of $\alpha(x_F)$ at $x_F > 0.25$.

The corresponding $\psi'$ calculations are compared to the data in Fig. 17 with the $S_3$ shadowing parametrization. For each absorption model, we show the $A$ dependence with the GM loss and the three estimates of BH loss. Because of the greater uncertainties in the data, none of the calculations are fully incompatible with the data at forward $x_F$. The largest discrepancies between model and data are at low to negative $x_F$. GM loss produces the largest $\alpha$ because of negligible loss effects at $x_F \approx 0$ combined with antishadowing. The minimum and original BH loss models agree relatively well with all the data for the three absorption models. Note that these two loss models coincide at large $x_F$ both because of their similar behavior at large $x_F$ (see Fig. 10), and the intrinsic charm contribution at forward $x_F$. All the calculations result in a slightly lower $\alpha$ for the $\psi'$ than the $\psi$ due to the larger comover cross section, $\sigma_{\psi' co}$.

The $A$ dependence of $\psi$ and $\psi'$ production has been shown to be similar in previous measurements [5], albeit not to high precision. To compare the two results here, we calculate the integrated $\alpha$ in the interval $-0.2 \leq x_F \leq 0.8$ for all energy loss models and all shadowing parametrizations. The results are shown in Tables II–IV. The change in $\alpha$ between $\psi$ and $\psi'$ at 800 GeV is small, typically a 2–3 % difference. One might expect that for pure octet absorption, the integrated $\alpha$ would be identical for $\psi$ and $\psi'$. However, the $pA$ comover interactions are treated assuming formed $\psi$ and $\psi'$ interact with secondaries and the $\psi'$ comover absorption cross section is larger. Thus, even though the comover interaction cross sections are typically significantly smaller than the corresponding nucleon absorption cross sections, the difference is large enough to cause the observed 2% shift in the integrated $\alpha$ in the tables. [See also Fig. 5(d) which highlights the differences in the assumed comover cross sections.] Indeed, without this difference in the cross sections, the model calculations would not agree as well with the data in Fig. 17.

We note that we do not expect our values of $\alpha$ to agree in detail with the integrated data because our estimates do not agree with the preliminary data at all $x_F$. The GM model always overestimates the data at low to negative $x_F$. Thus the GM results can then be expected to overestimate the integrated $\alpha$ of the data. Typical $\alpha$ values are between 0.94 and 0.98. The original and minimum estimates of BH loss typically underestimates the low and negative $x_F$ data and

---

[4]Gavin has addressed the E772 $\psi$ data with a combination of BH-type loss and shadowing without final-state effects and found a similar level of agreement as is seen here [66].
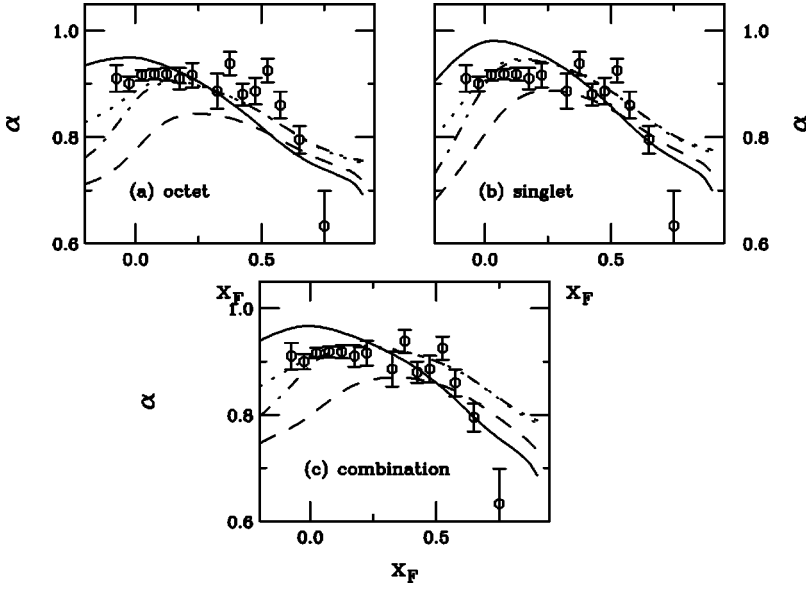
FIG. 17. All effects are combined and compared with the preliminary E866 $\psi'$ data [9]. In (a), pure octet absorption is assumed. The results for pure singlet absorption are given in (b) and combined octet/singlet absorption in (c). All calculations in (a) and (b) are in the CEM with the MRST LO parton densities, while the calculations in (c) are in NRQCD with the CTEQ 3L parton densities. The $S_3$ parametrization is used for calculations with different energy loss models. The GM loss is shown in the solid curve, while the dashed, dot-dashed, and dotted curves are calculations with the maximum, minimum, and original BH loss estimates, respectively.

should therefore underestimate the measured total $\alpha$. In this case, $0.87 < \alpha < 0.94$, similar to $\alpha = 0.91$ [5]. Even though the nuclear absorption cross sections are small, the effective absorption can be large, compatible with that obtained assuming absorption is the only source of the $\psi A$ dependence.

The integrated $\alpha$ also depends on the shadowing parametrization. Typically $\alpha$ with $S_2$ is largest with the octet absorption because the $S_2$ parametrization is not available for $A = 9$ and thus treats the Be nucleus like a proton. Therefore, although the $S_3$ parametrization has a larger gluon antishadowing effect than $S_2$, the calculated value of $\alpha$ is larger for $S_2$ near $x_F \approx 0$. This difference, along with smaller absorp-

tion cross sections used with $S_2$ (see Table I), results in a larger integrated $\alpha$ with $S_2$ for pure octet absorption (Table II). Since the $\psi$ and $\psi'$ are formed after they have left the nucleus in the pure singlet case at 800 GeV, the $\alpha$ obtained with $S_3$ is larger at this energy, see Table III. In the combination octet/singlet calculations (Table IV) $\alpha$ is very similar for $S_2$ and $S_3$.

A measurement of the $\psi A$ dependence at 120 GeV has been proposed. Such an energy would be the closest to the NA50 Pb+Pb measurement. The most precise lower energy data with a proton beam was taken at 200 GeV by the NA3 collaboration [3]. We compare our calculations of the ratio Pt/$^2$H to their data in Fig. 18. The three absorption mechanisms are shown with the data for GM loss and the three BH loss estimates with the $S_3$ shadowing parametrization. We see that essentially none of the calculations contradict the

TABLE II. The integrated value of $\alpha$ for $\psi$ and $\psi'$ production at 800 and 120 GeV assuming pure octet absorption. Note that $\alpha$ is integrated over the range $-0.2 \leq x_F \leq 0.8$ at both energies.

| Model | $S$ | $\psi$ 800 GeV | $\psi$ 120 GeV | $\psi'$ 800 GeV | $\psi'$ 120 GeV |
|---|---|---|---|---|---|
| GM | $S_1$ | 0.938 | 0.922 | 0.918 | 0.907 |
| | $S_2$ | 0.959 | 0.953 | 0.939 | 0.938 |
| | $S_3$ | 0.951 | 0.922 | 0.931 | 0.907 |
| KS | $S_1$ | 0.984 | 0.985 | 0.982 | 0.979 |
| | $S_2$ | 0.980 | 0.998 | 0.978 | 0.992 |
| | $S_3$ | 1.014 | 1.002 | 1.012 | 0.996 |
| Max BH | $S_1$ | 0.805 | 0.661 | 0.786 | 0.648 |
| | $S_2$ | 0.823 | 0.685 | 0.803 | 0.672 |
| | $S_3$ | 0.817 | 0.658 | 0.798 | 0.646 |
| Min BH | $S_1$ | 0.872 | 0.843 | 0.852 | 0.828 |
| | $S_2$ | 0.891 | 0.872 | 0.871 | 0.857 |
| | $S_3$ | 0.884 | 0.842 | 0.865 | 0.827 |
| Orig BH | $S_1$ | 0.890 | 0.850 | 0.870 | 0.836 |
| | $S_2$ | 0.908 | 0.875 | 0.888 | 0.864 |
| | $S_3$ | 0.903 | 0.851 | 0.883 | 0.836 |

TABLE III. The integrated value of $\alpha$ for $\psi$ and $\psi'$ production at 800 and 120 GeV assuming pure singlet absorption. Note that $\alpha$ is integrated over the range $-0.2 \leq x_F \leq 0.8$ at both energies.

| Model | $S$ | $\psi$ 800 GeV | $\psi$ 120 GeV | $\psi'$ 800 GeV | $\psi'$ 120 GeV |
|---|---|---|---|---|---|
| GM | $S_1$ | 0.958 | 0.916 | 0.933 | 0.882 |
| | $S_2$ | 0.968 | 0.944 | 0.944 | 0.914 |
| | $S_3$ | 0.983 | 0.924 | 0.957 | 0.886 |
| Max BH | $S_1$ | 0.829 | 0.658 | 0.805 | 0.631 |
| | $S_2$ | 0.833 | 0.679 | 0.811 | 0.655 |
| | $S_3$ | 0.854 | 0.661 | 0.830 | 0.632 |
| Min BH | $S_1$ | 0.894 | 0.840 | 0.870 | 0.808 |
| | $S_2$ | 0.901 | 0.865 | 0.878 | 0.836 |
| | $S_3$ | 0.920 | 0.846 | 0.895 | 0.811 |
| Orig BH | $S_1$ | 0.912 | 0.848 | 0.888 | 0.816 |
| | $S_2$ | 0.918 | 0.873 | 0.895 | 0.845 |
| | $S_3$ | 0.938 | 0.855 | 0.913 | 0.821 |

TABLE IV. The integrated value of $\alpha$ for $\psi$ and $\psi'$ production at 800 and 120 GeV assuming a combination of octet and singlet absorption. Note that $\alpha$ is integrated over the range $-0.2 \leq x_F \leq 0.8$ at both energies.

| Model | $S$ | $\psi$ | | $\psi'$ | |
|---|---|---|---|---|---|
| | | 800 GeV | 120 GeV | 800 GeV | 120 GeV |
| | $S_1$ | 0.948 | 0.939 | 0.926 | 0.917 |
| GM | $S_2$ | 0.977 | 0.983 | 0.955 | 0.963 |
| | $S_3$ | 0.978 | 0.956 | 0.954 | 0.929 |
| | $S_1$ | 0.804 | 0.597 | 0.788 | 0.583 |
| Max BH | $S_2$ | 0.831 | 0.637 | 0.814 | 0.625 |
| | $S_3$ | 0.835 | 0.612 | 0.816 | 0.593 |
| | $S_1$ | 0.880 | 0.830 | 0.863 | 0.817 |
| Min BH | $S_2$ | 0.907 | 0.872 | 0.890 | 0.860 |
| | $S_3$ | 0.911 | 0.847 | 0.892 | 0.830 |
| | $S_1$ | 0.899 | 0.853 | 0.881 | 0.835 |
| Orig BH | $S_2$ | 0.926 | 0.896 | 0.908 | 0.879 |
| | $S_3$ | 0.931 | 0.871 | 0.910 | 0.847 |

large $x_F$ data, presumably due to the relatively poor statistics for $x_F > 0.5$. The best agreement at all $x_F$ is obtained with minimum and original BH loss with the pure singlet and combination absorption models. GM loss tends to underestimate the low $x_F$ data. The maximum BH loss estimate produces a higher ratio at low $x_F$, as seen in Figs. 18(a) and 18(c), far above the data. On the whole, the results at 200 GeV concur with those at 800 GeV.

Figures 19 and 20 show the predictions for the $\psi$ and $\psi'$ $A$ dependence at 120 GeV. The calculations with GM loss show a plateaulike behavior at this energy and are very similar to each other over all $x_F$. This is due to the widening of the gluon antishadowing region over the $x_F$ interval (see Figs. 6–8). In the pure singlet model, since the $\psi$ and $\psi'$ may be produced inside the target at forward $x_F$, there is a peak in the calculated $\psi$ $\alpha(x_F)$ at $x_F \approx 0.2$ [see Fig. 19(b)].

This peak is shifted slightly forward for $\psi'$ production since the $\psi'$ singlet absorption cross section is larger [see Fig. 20(b)]. There is no forward $x_F$ peak when the octet model is considered because the nucleon absorption is treated identically at all $x_F$. Since the combination octet/singlet model includes both types of absorption, there is a rather wide plateau over $-0.2 < x_F < 0.3$. The shape of $\alpha(x_F)$ at 120 GeV could therefore help distinguish between absorption models. However, BH loss yields very different expectations at the lower energy. At low $x_F$, the BH loss calculations are governed by the decrease shown in Fig. 10. This effect is enhanced with singlet absorption since the $\psi$ and $\psi'$ have some probability to interact with their full cross sections. The maximum BH loss is so large that the first component of Eq. (2) is less than the intrinsic charm contribution so that rather than having a peak in $\alpha$ at low $x_F$, a minimum is seen instead. Results with the GM model and the minimum and original BH losses are similar for $x_F > 0.5$ due to intrinsic charm.

Note that at this energy, the integrated values of $\alpha$, also given in Tables II–IV, indicate that the differences between the $\psi$ and $\psi'$ $A$ dependence are again on the 2% level except when pure singlet absorption is considered. In the pure singlet case, the absorption cross section grows more slowly with $x_F$ at 120 GeV and some portion of the $\psi$ and $\psi'$ resonances are formed inside the target at $x_F > 0$. Even though the $\psi'$ formation time is larger than the $\psi$ formation time, the singlet absorption is larger for the $\psi'$ due to its increased cross section. High statistics measurements of the $\psi$ and $\psi'$ $A$ dependence at this energy would set bounds on the importance of singlet production of the resonances since there is a 3% difference in $\alpha$ between $\psi$ and $\psi'$ at 120 GeV in the singlet case. Note also that the $\psi$ and $\psi'$ octet and combination $A$ dependencies are within 1–2 % of each other at this energy, generally a smaller difference than at 800 GeV, because the comover density is lower.

It is typically assumed that the energy dependence of $\alpha$ is small. This is true for both the GM loss and the minimum and original BH loss estimates where $\alpha$ changes between 2
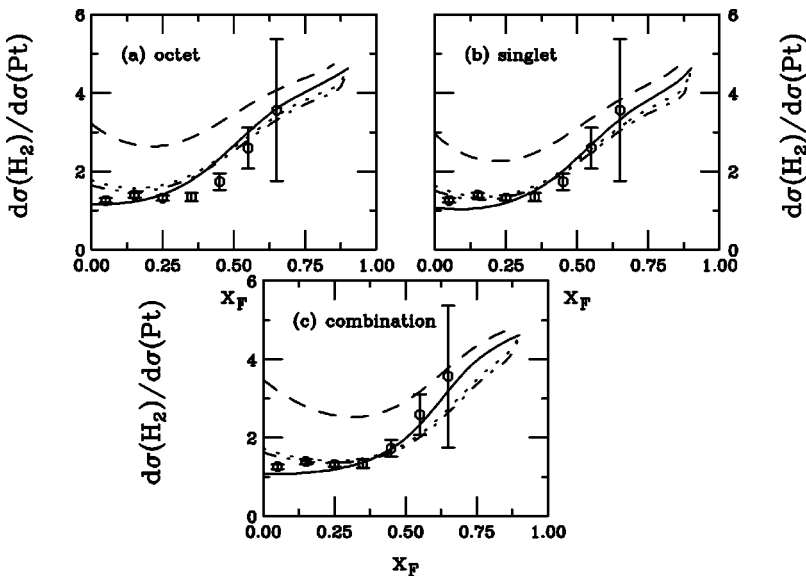


FIG. 18. All effects are combined and compared with the NA3 $\psi$ data [3]. In (a), pure octet absorption is assumed. The results for pure singlet absorption are given in (b) and combined octet/singlet absorption in (c). All calculations in (a) and (b) are in the CEM with the MRST LO parton densities, while the calculations in (c) are in NRQCD with the CTEQ 3$L$ parton densities. The $S_3$ parametrization is used for calculations with different energy loss models. The GM loss is shown in the solid curve, while the dashed, dot-dashed, and dotted curves are calculations with the maximum, minimum, and original BH loss estimates, respectively.
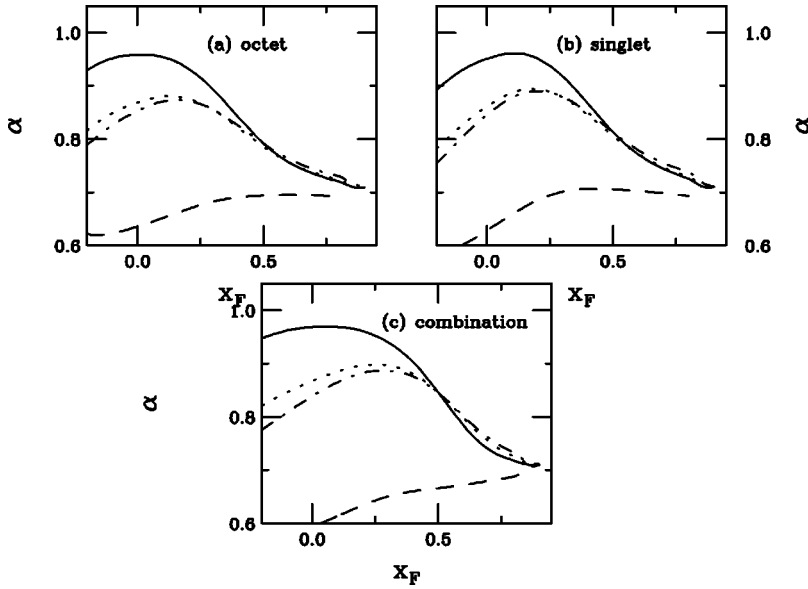
FIG. 19. Predictions are made for $\psi$ production at 120 GeV. In (a), pure octet absorption is assumed. The results for pure singlet absorption are given in (b) and combined octet/singlet absorption in (c). All calculations in (a) and (b) are in the CEM with the MRST LO parton densities, while the calculations in (c) are in NRQCD with the CTEQ 3$L$ parton densities. The $S_3$ parametrization is used for calculations with different energy loss models. The GM loss is shown in the solid curve, while the dashed, dot-dashed, and dotted curves are calculations with the maximum, minimum, and original BH loss estimates, respectively.

and 6 %. However, the energy dependence of the maximum BH loss is much stronger. There is a 10–25 % decrease of the integrated $\alpha$ with this estimate for the pure octet and singlet absorption mechanisms, as can be seen in Tables II and III. The energy dependence of the combination absorption model is typically stronger for all BH loss estimates because there is a stronger energy dependence of BH loss when $\psi$ production is calculated in NRQCD [compare Figs. 10(a) and 10(b)]. As seen in Table IV, the resulting energy difference in $\alpha$ is as large as 35% for the maximum BH estimate but is only 3–7 % for the lower BH loss estimates. Precision measurements of $\alpha$ at 800 and 120 GeV would
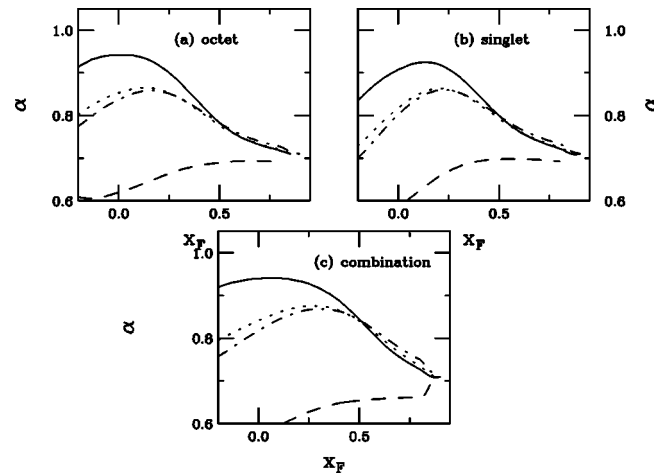


FIG. 20. Predictions are made for $\psi'$ $A$ dependence at 120 GeV. In (a), pure octet absorption is assumed. The results for pure singlet absorption are given in (b) and combined octet/singlet absorption in (c). All calculations in (a) and (b) are in the CEM with the MRST LO parton densities, while the calculations in (c) are in NRQCD with the CTEQ 3$L$ parton densities. The $S_3$ parametrization is used for calculations with different energy loss models. The GM loss is shown in the solid curve, while the dashed, dot-dashed, and dotted curves are calculations with the maximum, minimum, and original BH loss estimates, respectively.

help eliminate models. For example, the maximum BH loss could be ruled out but discerning the difference between the $A^{1/3}$ dependence of the loss in the original BH estimate and the $A^{2/3}$ dependence of the minimum BH loss [Eq. (38)], could be difficult.

Finally, we compare the difference between the Drell-Yan $A$ dependencies with shadowing and energy loss at 800 and 120 GeV in Figs. 21 and 22, respectively. Recall that the Drell-Yan mass range is $4 < M < 9$ GeV. All three shadowing parametrizations are shown for each energy loss estimate. We have included the E772 measurement of the Drell-Yan $A$ dependence based on D, Ca, Fe, and W targets [2] in Fig. 21. Since the GM loss parameter, $\epsilon_q$, is tuned to this data without shadowing, the full model calculation overestimates the $A$ dependence at large $x_F$. All the calculations with BH loss predict a significantly less than linear $A$ dependence for $x_F < 0$ at 800 GeV, as shown in Fig. 10. The maximum BH loss estimate is in complete disagreement with the E772 data which shows a rather mild $A$ dependence. The deviation of the model from the data in Fig. 21(b) suggests that the maximum estimated BH loss is certainly too large. Better agreement with the data is found with the original BH loss in Fig. 21(d) for the $S_1$ and $S_3$ shadowing parametrizations although the calculations consistently overestimate the $A$ dependence. When the difference in the color factors is included, the minimum BH quark loss, Eq. (38), agrees reasonably well with the data. Indeed, this model is the only one that follows the trend of the E772 data over all $x_F$.

The 120 GeV calculation shows a significant energy dependence of $\alpha$ when BH loss is considered. The $A$ dependence is now calculated for W and Be targets, as used in the E866 experiment. A precision measurement of $\alpha(x_F)$ at this energy could reveal if the $A$ dependence is less than linear here. There is, up to now, no data on the $A$ dependence of Drell-Yan production with a proton projectile below 200 GeV. A measurement of $\alpha$ at 200 GeV is for low masses, $1.7 < M < 2.7$ GeV [67]. Earlier measurements at lower energies are only available with pion beams [68,69]. The lowest
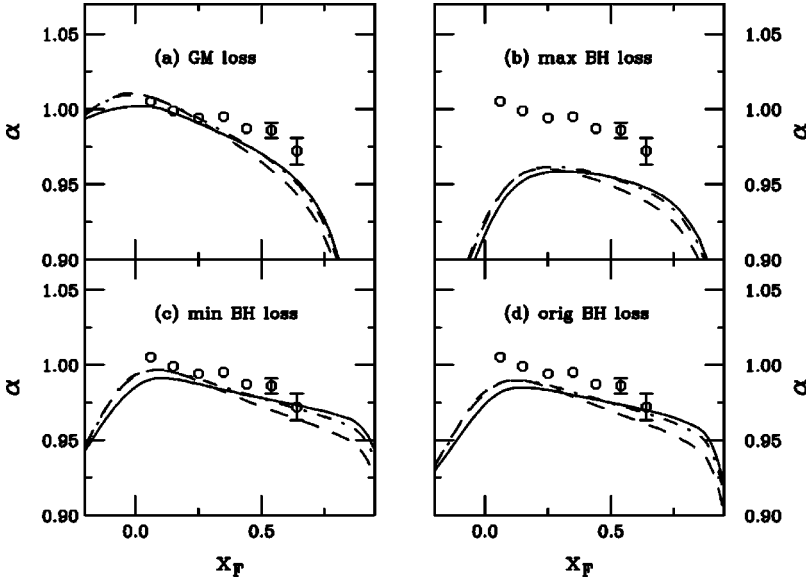
FIG. 21. Shadowing and energy loss in Drell-Yan production are combined and the $A$ dependence calculated for W and D targets, shown at 800 GeV. The E772 Drell-Yan $A$ dependence [2] is also shown. In (a), GM loss is assumed. Energy loss effects associated with the BH bound are shown in (b), (c), and (d) for the estimated maximum and minimum loss and the original bound, respectively. All calculations are with the MRST LO parton densities. The curves represent shadowing with the $S_3$ (solid), $S_2$ (dashed), and $S_1$ (dot-dashed) parametrizations.

energy pion beam data, at 140 GeV, obtained $\alpha = 0.980 \pm 0.006 \pm 0.013$ [68] which leaves room for a less than linear $A$ dependence at the lower proton beam energy. Other pion data below 280 GeV [69] does not have enough statistical significance to determine whether $\alpha$ deviates from unity at this energy, particularly at large $x_F$.

Since the E866 Drell-Yan data seems to indicate that only shadowing is necessary to explain the Drell-Yan $A$ dependence, in Fig. 23(a), we compare the E772 $A$ dependence with calculations of shadowing effects alone. All three shadowing parametrizations are in reasonable agreement with the data. That should be expected because the $S_2$ and $S_3$ parametrizations included these data in their fits. A comparison of Figs. 21(c) and 23(a) shows that the minimum BH quark loss has a very weak effect on the shape of $\alpha(x_F)$. The energy loss is only obvious in the curves at $x_F < 0.1$ and $x_F > 0.85$ and has little apparent influence on the agreement with the data. Thus, at least for this case, energy loss may be present but the effects nearly indistinguishable from those due to

shadowing alone. The 120 GeV predictions with shadowing only are shown in Fig. 23(b). Contrary to the results in Fig. 22, shadowing alone predicts a negligible influence on the $A$ dependence at the lower energy. A clear distinction can be made between models which include energy loss and those which do not with this measurement. Even a very small quark loss, such as that in the minimum BH quark loss estimate, causes the $A$ dependence to be less than linear at 120 GeV while shadowing alone would suggest that the $A$ dependence is either exactly linear or slightly greater than linear over all $x_F$. A high statistics measurement of the Drell-Yan $A$ dependence at 120 GeV could decisively settle the issue.

The integrated $\alpha$ values for all the calculations at 800 and 120 GeV assuming W and Be targets as in the E866 experiment are given in Table V. The choice of Be as the lowest mass target results in lower values of $\alpha$ than for a very light target like D since nuclear effects are larger in Be than D. When the GM loss is considered, all shadowing parametrizations are consistent with a 1% determination of $\alpha = 1$ at
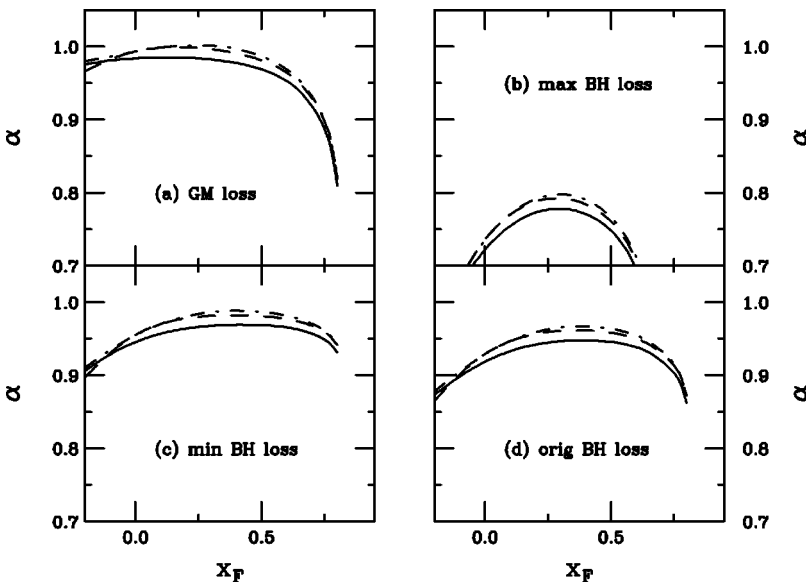


FIG. 22. Shadowing and energy loss in Drell-Yan production are combined and predictions of the $A$ dependence for W and Be targets given at 120 GeV. In (a), GM loss is assumed. Energy loss effects associated with the BH bound are shown in (b), (c), and (d) for the estimated maximum and minimum loss and the original bound, respectively. All calculations are with the MRST LO parton densities. The curves represent shadowing with the $S_3$ (solid), $S_2$ (dashed), and $S_1$ (dot-dashed) parametrizations.
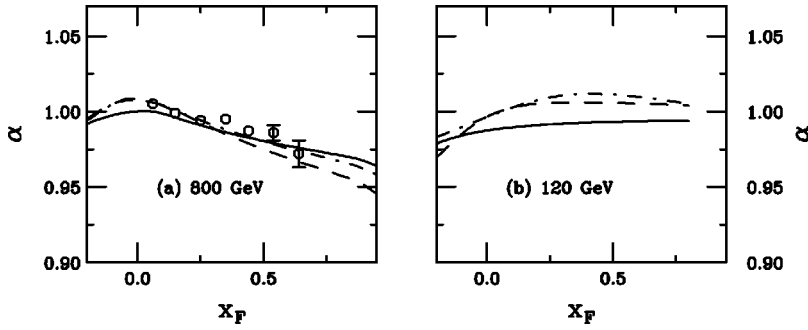
FIG. 23. Shadowing effects on Drell-Yan production at 800 (a) and 120 (b) GeV. All calculations are with the MRST LO parton densities. The curves represent shadowing with the $S_3$ (solid), $S_2$ (dashed), and $S_1$ (dot-dashed) parametrizations. Note that in (a), $\alpha$ is calculated with W and D targets for comparison with the E772 [2] data, while the calculations at 120 GeV assume W and Be targets.

800 GeV. At the lower energy, $\alpha$ is up to 2% away from unity with the $S_3$ parametrization. These results can be expected from the shadowing of the sea quark distributions in the "antishadowing" range, $0.1 < x < 0.3$, in the $S_3$ parametrization. [Compare Figs. 6(c) and 7(c) with Fig. 8(d).] If the original BH model is correct, a less than linear integrated $A$ dependence should already have been observed at 800 GeV. Since this is not the case, it seems that all but the minimum estimates are too large to explain the current Drell-Yan data. We note that even a reduced loss which agreed with the 800 GeV data would still predict $\alpha < 1$ at 120 GeV due to the energy dependence of the BH model which should be observable with high precision data. These results can be compared to the $\alpha$ predicted for shadowing alone, all compatible with unity at 120 GeV.

## X. CONCLUSIONS

In this paper we have tested a number of different nuclear effects: nuclear absorption, comover scattering, nuclear shadowing, energy loss, and the $A$ dependence of intrinsic charm. We have not attempted to make precise fits but rather check

TABLE V. The integrated value of $\alpha$ for Drell-Yan production at 800 and 120 GeV for different model assumptions. Note that $\alpha$ is integrated over the range $-0.2 \leq x_F \leq 0.8$ at both energies.

| Model | $S$ | 800 GeV | 120 GeV |
|-------|-----|---------|---------|
| | $S_1$ | 0.998 | 0.994 |
| GM | $S_2$ | 0.997 | 0.990 |
| | $S_3$ | 0.993 | 0.980 |
| | $S_1$ | 0.916 | 0.757 |
| Max BH | $S_2$ | 0.914 | 0.753 |
| | $S_3$ | 0.910 | 0.740 |
| | $S_1$ | 0.980 | 0.967 |
| Min BH | $S_2$ | 0.979 | 0.964 |
| | $S_3$ | 0.974 | 0.953 |
| | $S_1$ | 0.973 | 0.944 |
| Orig BH | $S_2$ | 0.972 | 0.941 |
| | $S_3$ | 0.968 | 0.930 |
| | $S_1$ | 0.997 | 1.002 |
| No loss | $S_2$ | 0.997 | 0.999 |
| | $S_3$ | 0.993 | 0.989 |

the resulting shape of $\alpha(x_F)$ for a number of processes that are expected to contribute to $\psi$ "suppression" in $pA$ collisions. The processes with the strongest influence on the $x_F$ dependence are shadowing and energy loss.

It is clear from the comparisons of the $\psi$ and $\psi'$ calculations with the data that a single mechanism cannot describe the shape of $\alpha(x_F)$ for all $x_F$. Combining all effects can explain some portion of the data, depending on which model of energy loss is assumed. A constant energy loss, á la Gavin and Milana [13], can describe the forward data when combined with the other effects discussed here but results in values of $\alpha$ too large at low $x_F$ due to gluon antishadowing.

An energy dependent model of energy loss, like that proposed by Brodsky and Hoyer [14] with refinements by Baier *et al.* [56,59], is less influenced by antishadowing because the dependence $\Delta x_1 \propto 1/x_1 s$ produces a strong $x_1$ shift at negative $x_F$, even strong enough to counteract the gluon antishadowing. At $x_F < 0$, the application of the model becomes problematic because $\Delta x_1$ grows larger than $x_1$. Therefore, the results in this region should be treated cautiously. This type of model alone fails to explain the data at larger $x_F$ because the $x_1$ shift becomes too small to cause a large enough change in the parton distributions for $x_F > 0.25$. The BH loss estimates are rather crude. For example, the minimum BH loss was calculated assuming that the gluon distribution in the proton remains relatively constant over the $x_1$ range of the data. If the nuclear gluon density as a function of $x_1$ was considered instead, the results may be more compatible with the data. It is unlikely, however, that such an effect could be significant at large $x_F$ since the gluon distribution decreases strongly at large $x_1$, thereby weakening the effect at large $x_F$. Thus if the BH model of energy loss is correct, a combination of BH loss and shadowing alone cannot describe the data, further strong absorption at large $x_F$ is still needed.

The apparently stronger absorption at large $x_F$ seen in the NA3 data [3] was the motivation for introducing $\psi$ production by hadronization of intrinsic charm states [20]. Indeed, without intrinsic charm, $\alpha(x_F)$ at large $x_F$ would be even further above the data (see Fig. 16). We have used an effective intrinsic charm production probability of 1%, within the uncertainties of the production probability determined from a fit to deep-inelastic scattering [65].

We have primarily used the MRST LO and CTEQ 3L parton densities in our calculations. While some deviations in the shape of $\alpha(x_F)$ appear for other sets of parton densities, these are not significant enough to change our general

conclusions. The most important effect in the determination of the $A$ dependence is the nature of the energy loss. Understanding this loss requires correlation of the $\psi$ $A$ dependence with that of other processes.

The preliminary data thus seem to suggest that final-state absorption, regardless of the mechanism, is not as strong as previously expected from studies of the integrated $A$ dependence [11] when other nuclear effects are included. A smaller cross section is needed than determined from absorption alone. This would be true even if comover effects are neglected since they are very small in $pA$ interactions. If the energy loss of quarks and gluons is treated on an equal footing, the BH loss mechanism results in a stronger $A$ dependence than required for the Drell-Yan data. Indeed, the minimum BH loss shows that treating the energy loss of quarks and gluons separately can lead to qualitative agreement with the $\psi$ and Drell-Yan $A$ dependence.

Further data on the $A$ dependence at 120 GeV could clarify the relative importance of octet and singlet states in the production and absorption of the charmonium states. A Drell-Yan measurement at this energy may decisively determine the importance of energy loss by the initial partons. In addition, precision measurements of the $x_F$ dependent absolute cross sections in $pp$ collisions could show whether the $x_F$ distribution is closer to that expected from the CEM or NRQCD.

The lower energy data can also provide an additional point of comparison to the NA50 measurements of $\psi$ suppression in heavy-ion collisions at the CERN SPS [7]. Only nuclear absorption and some comover scattering has been used to compare to the $x_F$-integrated data [7,10,11]. Shadowing should also be included in the analysis [70]. Interestingly, the $\alpha(x_F)$ extracted from the E866 800 GeV data [9] in the NA50 $x_F$ region is larger than that obtained by NA50 between 158 and 450 GeV [7]. An independent measurement at a similar energy could be very valuable.

[1] J.C. Collins, D.E. Soper, and G. Sterman, in *Perturbative Quantum Chromodynamics*, edited by A.H. Mueller (World Scientific, Singapore, 1989), p. 1.
[2] D.M. Alde *et al.*, E772 Collaboration, Phys. Rev. Lett. **64**, 2479 (1990).
[3] J. Badier *et al.*, NA3 Collaboration, Z. Phys. C **20**, 101 (1983).
[4] S. Katsanevas *et al.*, E537 Collaboration, Phys. Rev. Lett. **60**, 2121 (1988).
[5] D.M. Alde *et al.*, E772 Collaboration, Phys. Rev. Lett. **66**, 133 (1991).
[6] M.J. Leitch *et al.*, E789 Collaboration, Nucl. Phys. **A544**, 197c (1992).
[7] M.C. Abreu *et al.*, NA50 Collaboration, Phys. Lett. B **410**, 327 (1997); **410**, 337 (1997).
[8] M.J. Leitch, E866 Collaboration, in *Quarkonium Production in Relativistic Nuclear Collisions*, edited by X.-N. Wang and B. Jacak (World Scientific, Singapore, 1999), p. 42.
[9] M.J. Leitch, E866 Collaboration, in Proceedings of ''Quark Matter '99,'' Torino, Italy, 1999, edited by L. Riccati *et al.*; nucl-ex/9909007 (submitted to Phys. Rev. Lett.).
[10] R. Vogt, Phys. Lett. B **430**, 15 (1998).
[11] D. Kharzeev, C. Lourenço, M. Nardi, and H. Satz, Z. Phys. C **74**, 307 (1997).
[12] J.J. Aubert *et al.*, Nucl. Phys. **B293**, 740 (1987); M. Arneodo, Phys. Rep. **240**, 301 (1994).
[13] S. Gavin and J. Milana, Phys. Rev. Lett. **68**, 1834 (1992).
[14] S.J. Brodsky and P. Hoyer, Phys. Lett. B **298**, 165 (1993).
[15] S. Gavin and R. Vogt, Nucl. Phys. **B345**, 104 (1990).
[16] N. Armesto, in Proceedings of the 32nd Rencontres de Moriond, ''QCD and High Energy Hadronic Interactions,'' Les Arcs, France, 1997; N. Armesto and A. Capella, Phys. Lett. B **430**, 23 (1998).
[17] D. Kharzeev and H. Satz, Z. Phys. C **60**, 389 (1993).
[18] S.J. Brodsky, P. Hoyer, C. Peterson, and N. Sakai, Phys. Lett. **93B**, 451 (1980); S.J. Brodsky, C. Peterson, and N. Sakai, Phys. Rev. D **23**, 2745 (1981).
[19] S.J. Brodsky and P. Hoyer, Phys. Rev. Lett. **63**, 1566 (1989).
[20] R. Vogt, S.J. Brodsky, and P. Hoyer, Nucl. Phys. **B360**, 67 (1991).
[21] R.V. Gavai *et al.*, Int. J. Mod. Phys. A **10**, 3043 (1995).
[22] V. Barger, W.Y. Keung, and R.N. Philips, Z. Phys. C **6**, 169 (1980); Phys. Lett. **91B**, 253 (1980).
[23] R. Vogt, Phys. Rep. **310**, 197 (1999).
[24] A.D. Martin, R.G. Roberts, and W.J. Stirling, and R.S. Thorne, Eur. Phys. J. C **4**, 463 (1998); Phys. Lett. **B443**, 301 (1998).
[25] A. Sansoni, CDF Collaboration, Nucl. Phys. **A510**, 373c (1996).
[26] C. Lourenço *et al.*, NA38/NA50 Collaboration, in Proceedings of the EPS International Conference on High Energy Physics, Brussels, Belgium, 1995, EPS HEP Conference 1995:363, CERN-PRE-95-001.
[27] L. Antoniazzi *et al.* E705 Collaboration, Phys. Rev. Lett. **70**, 383 (1993); Phys. Rev. D **46**, 4828 (1992).
[28] B. Ronceux, NA38 Collaboration, Nucl. Phys. **A566**, 371c (1994).
[29] M.L. Mangano, P. Nason, and G. Ridolfi, Nucl. Phys. **B405**, 507 (1993).
[30] G.A. Schuler and R. Vogt, Phys. Lett. B **387**, 181 (1996).
[31] R. Baier and R. Rückl, Z. Phys. C **19**, 251 (1983); G.A. Schuler, CERN Preprint CERN-TH.7170/94.
[32] F. Abe *et al.*, CDF Collaboration, Phys. Rev. Lett. **71**, 3421 (1993).
[33] G.T. Bodwin, E. Braaten, and G.P. Lepage, Phys. Rev. D **51**, 1125 (1995).

[34] M. Beneke and I.Z. Rothstein, Phys. Rev. D **54**, 2005 (1996).

[35] H.L. Lai *et al.*, Phys. Rev. D **51**, 4763 (1995).

[36] S. Gavin *et al.*, Int. J. Mod. Phys. A **10**, 2961 (1995).

[37] D. Kharzeev and H. Satz, Phys. Lett. B **366**, 316 (1996).

[38] C.W. deJager, H. deVries, and C. deVries, At. Data Nucl. Data Tables **14**, 485 (1974).

[39] F. Karsch, M.T. Mehr, and H. Satz, Z. Phys. C **37**, 617 (1988).

[40] J.-P. Blaizot and J.-Y. Ollitrault, Phys. Lett. B **217**, 386 (1989).

[41] L. Gerland, L. Frankfurt, M. Strikman, H. Stöcker, and W. Greiner, Phys. Rev. Lett. **81**, 762 (1998).

[42] J. Hüfner and B. Povh, Phys. Rev. Lett. **58**, 1612 (1987).

[43] X.-F. Zhang, C.-F. Qiao, X.-A. Yao, and W.-Q. Chao, hep-ph/9711237; X.-F. Zhang, in *Quarkonium Production in Relativistic Nuclear Collisions*, edited by X.-N. Wang and B. Jacak (World Scientific, Singapore, 1999), p. 111.

[44] J.D. Bjorken, Phys. Rev. D **27**, 140 (1983).

[45] F. Abe *et al.*, CDF Collaboration, Phys. Rev. D **41**, 2330 (1990); K. Alpgård *et al.*, Phys. Lett. **115B**, 71 (1982).

[46] M.R. Adams *et al.*, Phys. Rev. Lett. **68**, 3266 (1992).

[47] V. Emel'yanov, A. Khodinov, S.R. Klein, and R. Vogt, Phys. Rev. Lett. **81**, 1801 (1998); V. Emel'yanov, A. Khodinov, S.R. Klein, and R. Vogt, Phys. Rev. C **56**, 2726 (1997).

[48] K.J. Eskola, J. Qiu, and J. Czyzewski (private communication).

[49] K.J. Eskola, Nucl. Phys. **B400**, 240 (1993).

[50] D.W. Duke and J.F. Owens, Phys. Rev. D **30**, 49 (1984).

[51] M. Glück, E. Reya, and A. Vogt, Z. Phys. C **53**, 127 (1993).

[52] K.J. Eskola, V.J. Kolhinen, and P.V. Ruuskanen, Nucl. Phys. **B535**, 351 (1998).

[53] K.J. Eskola, V.J. Kolhinin, and C.A. Salgado, Eur. Phys. J. C **9**, 61 (1999).

[54] A. Baldit *et al.*, NA51 Collaboration, Phys. Lett. B **332**, 244 (1994).

[55] X.-N. Wang and M. Gyulassy, Phys. Rev. Lett. **68**, 1480 (1992); R. Baier, Yu.L. Dokshitser, S. Peigne, and D. Schiff, Phys. Lett. B **345**, 277 (1995); R. Baier, Yu.L. Dokshitser, A.H. Mueller, S. Peigne, and D. Schiff, Nucl. Phys. **B478**, 577 (1996); **B483**, 291 (1997); M.G. Mustafa, D. Pal, D.K. Srivastava, and M.H. Thoma, Phys. Lett. B **428**, 234 (1998).

[56] R. Baier, Yu.L. Dokshitser, A.H. Mueller, S. Peigne, and D. Schiff, Nucl. Phys. **B484**, 265 (1997).

[57] J.F. Gunion, Phys. Lett. **88B**, 150 (1979).

[58] L.D. Landau and I.Ya. Pomeranchuk, Dokl. Akad. Nauk SSSR **92**, 535 (1953); **92**, 735 (1953); A.B. Migdal, Phys. Rev. **103**, 1811 (1956).

[59] R. Baier, Yu.L. Dokshitser, A.H. Mueller, and D. Schiff, Nucl. Phys. **B531**, 403 (1998).

[60] B.G. Zakharov, Pis'ma Zh. Éksp. Teor. Fiz. **62**, 906 (1996) [JETP Lett. **63**, 952 (1996)]; **65**, 585 (1997) [**65**, 615 (1997)]; Yad. Fiz. **61**, 924 (1998) [Phys. At. Nucl. **61**, 838 (1998)].

[61] M. Luo, J. Qiu, and G. Sterman, Phys. Rev. D **49**, 4493 (1994).

[62] S.J. Brodsky, P. Hoyer, A.H. Mueller, and W.-K. Tang, Nucl. Phys. **B369**, 519 (1992).

[63] R. Vogt and S.J. Brodsky, Phys. Lett. B **349**, 569 (1995).

[64] J.J. Aubert *et al.*, EMC Collaboration, Phys. Lett. **110B**, 73 (1982); E. Hoffmann and R. Moore, Z. Phys. C **20**, 71 (1983).

[65] B.W. Harris, J. Smith, and R. Vogt, Nucl. Phys. **B461**, 181 (1996).

[66] S. Gavin (private communication).

[67] C. Baglin *et al.*, NA38 Collaboration, Phys. Lett. B **270**, 105 (1991).

[68] P. Bordalo *et al.*, NA10 Collaboration, Phys. Lett. B **193**, 368 (1987); **193**, 373 (1987).

[69] H.J. Frisch *et al.*, Phys. Rev. D **25**, 2000 (1982); A. Michelini, in Proceedings of the EPS International Conference on High Energy Physics, Lisbon, Portugal, 1981, EPS HEP Conference 1981:261; S. Falciano, Phys. Lett. **104B**, 416 (1981).

[70] V. Emel'yanov, A. Khodinov, S.R. Klein, and R. Vogt, Phys. Rev. C **59**, 1860 (1999).